land

MDPI

Article

Combining Soil Moisture and MT-InSAR Data to Evaluate Regional Landslide Susceptibility in Weining, China

Qing Yang [1], Zhanqiang Chang [2,3], Chou Xie [4,5,6,*], Chaoyong Shen [7,*], Bangsen Tian [4,6], Haoran Fang [4,5], Yihong Guo [4], Yu Zhu [4], Daoqin Zhou [7], Xin Yao [7], Guanwen Chen [7] and Tao Xie [7]

1 China Siwei Surveying and Mapping Technology Co., Ltd., Beijing 100086, China; qyoung1997@cnu.edu.cn
2 College of Resource, Environment &Tourism, Capital Normal University, Beijing 100048, China
3 Key Lab of 3D Information Acquisition of Education Ministry of China, Beijing 100048, China
4 Aerospace Information Research Institute, Chinese Academy of Sciences, Beijing 100101, China; tianbs@aircas.ac.cn (B.T.); fanghaoran19@mails.ucas.an.cn (H.F.)
5 University of Chinese Academy of Sciences, Beijing 100049, China
6 Laboratory of Target Microwave Properties, Deqing Academy of Satellite Applications, Deqing 313200, China
7 The Third Surveying and Mapping Institute of Guizhou Province, Guiyang 550004, China
* Correspondence: xiechou@aircas.ac.cn (C.X.); shency@gzchsy.cn (C.S.)

Abstract: Landslide susceptibility maps (LSMs) play an important role in landslide hazard risk assessments, urban planning, and land resource management. While states of motion and dynamic factors are critical in the landslide formation process, these factors have not received due attention in existing LSM-generation research. In this study, we proposed a valuable method for dynamically updating and refining LSMs by combining soil moisture products with Multi-Temporal Interferometric Synthetic Aperture Radar (MT-InSAR) data. Based on a landslide inventory, we used time-series soil moisture data to construct an index system for evaluating landslide susceptibility. MT-InSAR technology was applied to invert the displacement time series. Furthermore, the surface deformation rate was projected in the direction of the steepest slope, and the data was resampled to a spatial resolution consistent with that of the LSM to update the generated LSM. The results showed that varying soil moisture conditions were accompanied by dynamic landslide susceptibility. A total of 22% of the analyzed pixels underwent significant susceptibility changes (either increases or decreases) following the updating and refining processes incorporating soil moisture and MT-InSAR compared to the LSMs derived based only on static factors. The relative landslide density index obtained based on actual landslides and the analyses of Dongfeng, Haila town, and Dajie township confirmed the improved slow landslide prediction reliability resulting from the reduction of the false alarm and omission rates.

Keywords: dynamic landslide susceptibility; MT-InSAR; soil moisture

Citation: Yang, Q.; Chang, Z.; Xie, C.; Shen, C.; Tian, B.; Fang, H.; Guo, Y.; Zhu, Y.; Zhou, D.; Yao, X.; et al. Combining Soil Moisture and MT-InSAR Data to Evaluate Regional Landslide Susceptibility in Weining, China. *Land* **2023**, *12*, 1444. https://doi.org/10.3390/land12071444

Academic Editors: Candide Lissak, Christopher Gomez and Vittoria Vandelli

Received: 9 June 2023
Revised: 11 July 2023
Accepted: 13 July 2023
Published: 20 July 2023

1. Introduction

According to the data published in the "China Statistical Yearbook 2021", more than 100,000 geological disasters occurred in China from 2010 to 2020, causing approximately 8200 casualties and economic losses of 6.92 billion dollars [1]. Landslides are among the most destructive natural disasters and occur frequently worldwide, resulting in serious casualties, property losses, and infrastructure losses [2]. Therefore, it is necessary to not only scientifically assess the potential locations and areas that are vulnerable to landslides but also to purposefully fulfill early monitoring, early warning, and risk control measures, as these are indispensable means and components in the disaster prevention and mitigation processes [3–5]. Landslide susceptibility is defined as the likelihood of a landslide occurring in a certain area based on the local terrain conditions [6]; thus, this measure represents the possibility that an area may be affected by landslide disasters in the future [7]. A scientific

and reliable landslide susceptibility map (LSM) can effectively predict the spatial distribution and probability of occurrence of landslides. LSMs provide a basis for landslide disaster risk assessments, landslide management, urban planning, and land resource management.

The occurrence of landslides is affected by internal factors that determine the soil structure and slope stability and by external factors that change the soil shear strength. At present, most studies that have focused on the correlations between landslides and their influencing factors have adopted the methodology of constructing different landslide susceptibility prediction models [8–10]. According to the intrinsic properties of these influencing factors, they can be divided into four aspects: geological, topographic, environmental factors, and human engineering activities [11,12]. However, researchers have mostly used static or relatively stable factors that change very little over long periods, such as factors representing the lithology, slope, slope aspect, land cover, elevation, distance from rivers, and distance from roads of an area.

To generate targeted LSMs and expect regular LSM updates to achieve near-real-time or even real-time landslide predictions, some researchers have discussed using the conjoint analysis technique by incorporating instances of landslides and information representing unstable factors. These factors may cause significant temporal and spatial changes, as extracted by seismic activity and precipitation data. Most ordinary real-time landslide forecasting methods rely on rainfall thresholds [13–15]. However, early landslide warnings derived based exclusively on rainfall thresholds may not be reliable due to the lack of soil moisture condition information, as soil moisture plays a crucial role in the occurrence of landslides. Some studies have simulated soil moisture using the antecedent precipitation index (API) [16,17]. Nevertheless, this methodology has not been accepted from some points of view [18], considering the process by which water conditions change over time: after precipitation reaches the land surface, a portion of the water enters the soil layer, a portion becomes runoff [19], and the final portion returns to the atmosphere through evapotranspiration. These factors lead to a weak relationship between previous precipitation and shifting soil moisture conditions. Thus, drawing conclusions from actual soil moisture information represents an improved solution in landslide susceptibility research [20–23].

The soil moisture value can be obtained through field investigations, surface or hydrological model estimations, or remote sensing inversions [18]. Although field investigations provide the highest accuracies among these three methods, they provide only point-based measurement data, and it is difficult to establish a dense measurement network covering a large area using this method due to the high installation and maintenance costs of the instruments. The model estimation methods frequently encounter a series of problems, including error accumulation, the required input of a large amount of accurate data, and normally intensive calculations. Consequently, satellite remote sensing inversion methods could offer a wide range of continuously observed soil moisture data that is in good agreement with field measurements [24–26]. A previous study showed that the Soil Moisture Active Passive (SMAP) L4 root zone soil moisture product has great potential in landslide susceptibility evaluations [27].

Generally, a certain period of time is required from the deformation process to the moment of failure during the formation of a landslide. The evolution of surface deformation over time characterizes the motion states of landslides [28], thus enabling the identification of landslide hazard precursors [29]. The Multi-Temporal Interferometric Synthetic Aperture Radar (MT-InSAR) is an interferometric SAR measurement technology that has already been confirmed as capable of researching, monitoring, and investigating regionally slow-moving landslides due to its all-time, large-scale, and high-precision characteristics [30–33]. This technology has been widely applied in landslide investigations; despite this, quantitative and susceptibility analyses of landslide hazards are rare. A few studies have confirmed the applicability of a combination of MT-InSAR technology with an LSM [30,34–36].

To fill this gap and improve the applicability of LSMs, updated LSMs should contain various dynamic information, such as regional deformation information and soil moisture information. In past studies, researchers have implemented MT-InSAR and soil moisture

data to conduct landslide susceptibility assessments; however, no past work has utilized these data simultaneously. In this study, we proposed a new procedure that can be used to conduct large-area landslide susceptibility mapping while integrating soil moisture products and MT-InSAR deformation data. We took Weining County, Bijie City, Guizhou Province, as the study area. A total of 13 influencing factors related to environmental conditions, including soil moisture, were used to construct the dynamic landslide susceptibility evaluation system. On this basis, a random forest (RF) model was utilized to evaluate the landslide susceptibility and create the initial dynamic LSM to be further refined. The model was then verified using the area under the receiver operating curve (ROC) (AUC) value, accuracy rate, precision rate, recall rate, and F-measure values as the evaluation indicators. A LSM refined by the MT-InSAR dataset was obtained as the output of this processing approach, providing the landslide occurrence susceptibility distribution with relatively low false alarm and omission rates.

2. Study Area

Weining County, the study area, spans longitude lines from approximately 103°36′ to 104°45′ E and latitude lines from 26°36′ to 27°26′ N on the northwestern edge of Guizhou Province (Figure 1). It has a wavering climate, a complex geological structure, and diverse landform types, making it one of the most vulnerable areas in Guizhou Province with regards to the ecological environment [37]. The sedimentary strata in this area are relatively well developed, and only Ordovician, Silurian, Lower Permian, Cretaceous, and Paleogene strata are missing. Among the present strata, the Sinian, Devonian, Carboniferous, Permian, and Triassic contain extensive distributions of carbonate rocks with a maximum cumulative thickness of 3800 m. The total thickness of sedimentary rocks from the Proterozoic Sinian to the Cenozoic is more than 10,000 m. Tectonically, the tectonostratigraphic framework is shaped by the Himalayan movement, and its changes are controlled by the Yanshan movement. Three main groups of structures span across the northeast, northwest, and near-north-south directions, roughly radiating in parallel fold axes from the central Caohai area and being unceasingly accompanied by compressive torsional strike faults [38,39]. Weining is the largest-area and highest-elevation county in Guizhou Province due to its area coverage of 6298 km^2 and average elevation of 2237 m. The Wumeng Mountains run through the county, containing four peaks over 2800 m tall. The terrain over this county is generally high in the west and low in the east, and the central region is a substantially elevated, open, and gently sloping plateau. The groundwater conditions mainly depend on the infiltration and recharge of precipitation that contains mainly carbonate karst water, followed by bedrock fissure water, while small amounts of pore water are present in loose accumulations [40].

The background of these special natural geographical and geological environments, coupled with the rapid social and economic development of this county in recent years, has accelerated the transformation of the geological environment alongside human engineering activities, thus directly or indirectly leading to the frequent occurrence of various geological disasters and causing vast economic losses. On 19 September 2006, a landslide occurred in the Dengjiaying section of Niupeng Town, Weining; tens of thousands of rocks and stones collapsed, causing interruptions and blockages of the Nei-Kun Railway. On 18 September 2008, a landslide occurred in Qinghe Village, Bandi Township, Weining, due to torrential rain, killing six people and destroying five houses. On 21 July 2019, a landslide occurred in Yancang town, Weining County, endangering 34 households and 178 people.

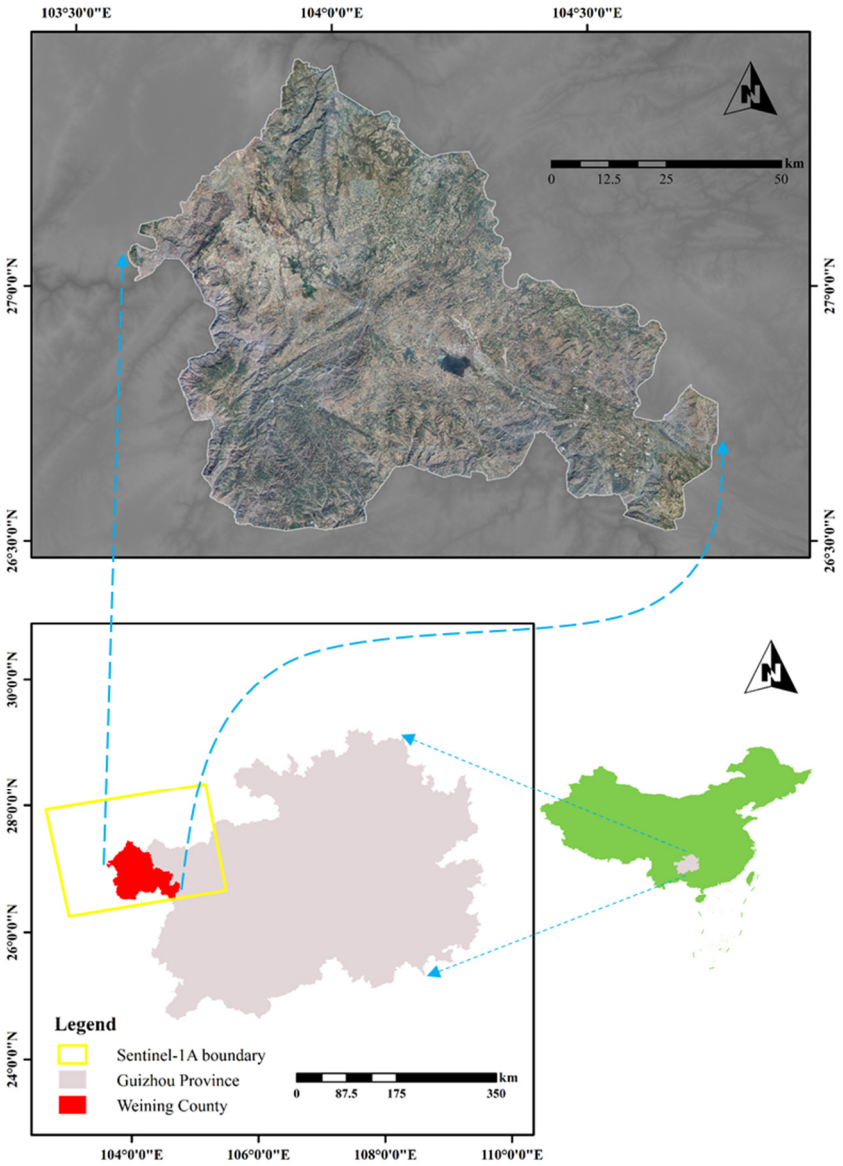

Figure 1. Location of the study area.

3. Data

3.1. Landslide Inventory

Landslide inventory datasets are crucial for landslide susceptibility mapping and also serve as the basis for future landslide prediction and analysis research. By January 2019, 118 landslides had been recorded in Weining, and a total of 140 landslides had been registered until January 2020, according to the geological survey, indicating an increase of 22 landslides in 2019. The landslide inventory was derived from the field geological investigation report (provided by the Guizhou Geological Environment Monitoring Institute). These landslide cases are primarily caused by natural factors, and among them, soil landslides account for approximately 95%, which indicates the suitability for the following research.

3.2. Landslide Influencing Factors

The landslide formation mechanism is deeply complex, and the occurrence of a landslide is caused by a variety of influencing factors [41]. The critical factors to consider when performing landslide susceptibility evaluations depend on the local characteristics of the study area, the landslide type, the major triggers, the data availability, and the chosen

modeling method [42]. Based on previous landslide inventory analyses, natural factors have been found to be the dominant factors affecting the occurrence of landslides in the study area, and the major types of landslides are small or medium-sized soil landslides. Through the examination of a large number of studies, the availability and correlation of the obtained data were carefully analyzed. We adopted the following 13 influencing factors in the LSM generation process [6,43]: the curvature, plane curvature, profile curvature, elevation, slope, aspect, distance from faults, lithology, land cover, soil moisture, NDVI, TRI, and LR, which were characterized in four aspects, topographic conditions, geological conditions, environmental factors, and human engineering activities, to establish a landslide susceptibility evaluation index system, as shown in Table 1.

Table 1. Factors affecting landslides.

Influencing Factor	Source	Scale/Resolution
Lithology	Geological map of Weining	1:500,000
Distance from faults (m)	Geological map of Weining	1:500,000
Elevation (m)	Digital elevation model (DEM)	30 × 30 m
Slope (°)	Digital elevation model (DEM)	30 × 30 m
Aspect	Digital elevation model (DEM)	30 × 30 m
Curvature	Digital elevation model (DEM)	30 × 30 m
Profile curvature	Digital elevation model (DEM)	30 × 30 m
Plan curvature	Digital elevation model (DEM)	30 × 30 m
TRI (Terrain Roughness Index)	Digital elevation model (DEM)	30 × 30 m
LR (Land Relief)	Digital elevation model (DEM)	30 × 30 m
NDVI (Normalized Difference Vegetation Index)	Landsat	30 × 30 m
Land cover	GlobeLand30 (http://www.globallandcover.com/)	30 × 30 m
Soil moisture	National Aeronautics and Space Administration (NASA) National Snow and Ice Data Center Distributed Active Archive Center	9 × 9 km

3.2.1. Geological Factors

Lithology is a crucial factor in the progression of landslide formation, especially in mountainous areas. Different lithological units are equivalent to diverse degrees of permeability and strength in rocks as well as in soils [39,40]. Furthermore, landslides are more likely to occur in low-permeability areas than in highly permeable areas. The distance from faults is another common factor involved in landslide susceptibility mapping, and this factor also plays an important role in slope deformation. Generally, within a certain range, the closer an area is to a fault, the lower the rock strength is and the stronger the soil is. The looser the soil is, the higher the probability of landslides occurring.

The lithology of the study area is dominated by limestone in the central region, with small amounts of clay rock, carbonate rock, and basalt spreading from the center to the surrounding areas. Roughly taking the Caohai area as the center of the study area, three groups of faults radiate from the northeast, northwest, and near-north-south directions.

3.2.2. Topographic Factors

Because landslides are strongly correlated with elevation, slope, aspect, and curvature, these factors are often used in landslide susceptibility studies [44,45]. In mountainous areas, external conditions such as rainfall, vegetation cover, and human activities are related to elevation and affect the occurrence of landslides [46]. The slope represents the maximum gradient from the target pixel to the adjacent pixels. The smaller the slope, the flatter the terrain is, and vice versa [47]. The aspect is the downslope direction corresponding to the largest gradient from each cell to its neighboring cells [47]. Curvature can be used to characterize the physics of watershed basins, thus facilitating the understanding of erosion processes and runoff formation. The profile curvature affects the acceleration and deceleration of runoff, which in turn affects erosion and vegetation growth. The plane curvature is related to the convergence and divergence of runoff on the land surface [48].

The TRI is commonly defined as the ratio of the surface unit area to its projected area on a horizontal plane. Roughness is a macrotopographic factor that can reflect terrain fluctuations and erosion. The higher the roughness coefficient, the more serious the erosion degree [46]. The LR refers to the difference between the elevations of the highest and lowest points in a specific area. This term is a macro index that describes the terrain features of a region and can be applied to assist in terrain classification tasks [49].

The overall terrain of Weining is high in the west and low in the east, and high in the middle and low in the surrounding areas, with an average elevation of approximately 2137 m and a maximum elevation difference of 1636 m. Each curvature profile shows a phenomenon in which that in the central region is small and that in the surrounding area is high. The average slope is approximately 16.5°, and approximately 77.81% of the study area corresponds to slopes between 6° and 25°; in addition, the slope aspect is equally distributed throughout the study area.

3.2.3. Environmental Factors

The NDVI has long been regarded as a factor representing vegetation characteristics in susceptibility zoning studies and is a weighty factor reflecting vegetation growth and coverage; this factor is closely related to the seepage, runoff, and weathering of slopes [50]. Land cover is a factor frequently considered in LSM research; this factor can describe the type of vegetation cover and can also reflect human engineering and production activities [51].

The NDVI and land cover data in this study were extracted from the Landsat and GlobeLand30 [52] datasets, respectively. In addition, the vegetation coverage in the study area is quite high, with forestlands, shrubs, and grasslands serving as the main land cover types. The forestland coverage rate is over 40%, and the average NDVI value is approximately 0.56.

3.2.4. Soil Moisture

Soil moisture critically impacts the formation and morphology of landslides. For soil or rock slopes that are easily softened by water, high water contents can weaken the connection between soil particles or rocks. That is, the suction among the soil elements decreases, resulting in a decrease in the shear strength of the soil or rock mass and leading to the occurrence of landslides. We employed the SMAP product to characterize the shallow surface water content. SMAP, an environmental monitoring satellite launched by the National Aeronautics and Space Administration (NASA) on 31 January 2015, is the latest in-orbit satellite dedicated to measuring soil moisture [53]. The SMAP carries a radiometer sensor (passive) and a SAR sensor (active). The method of combining active and passive measurements takes advantage of the spatial resolution of radar and the perception accuracy of radiometers.

The data is divided into four processing levels:

- Level-1 products contain instrument-related data.
- Level-2 products are derived from the geophysical inversion results obtained based on instrument data.
- Level-3 products are the daily global composite data of the Level-2 products synthesized over each Coordinated Universal Time (UTC) day, obtained by resampling the Level-2 product to the global grid.
- The Level-4 products contain root-zone soil moisture estimates obtained by assimilating SMAP observations into a surface model.

In this study, we obtained the SMAP L4 Global 3-hourly 9-km EASE-Grid Surface and Root Zone Soil Moisture Geophysical Data, Version 5, from 2017 to 2019, characterizing the soil moisture in the root zone (at average depths of 0–100 cm in the vertical direction) (SMAP-R); the unit is the water content per unit volume (m^3/m^3) [54]. In the time series, the soil moisture within the county exhibits a distribution pattern of low values in the middle and high values in the surrounding areas.

3.3. SAR Data

In this paper, we utilized Sentinel-1 data to perform the MT-InSAR deformation analysis. Sentinel-1 is a two-satellite (Sentinel-1A and Sentinel-1B) Earth observation satellite constellation in the European Space Agency's Copernicus Global Monitoring for Environment and Security (GMES) program carrying a C-band synthetic aperture radar; its working wavelength is 5.5 cm. The two-satellite constellation offers a 6-day exact cycle at the equator. In this work, we conducted an MT-InSAR analysis with 31 imageries covering one scene. These SAR imageries were recorded in interferometric wide (IW) swath mode at a 20-m ground resolution, 240-km swath width, and VV polarization. The relevant parameters are listed in Table 2.

Table 2. Main acquisition parameters of the Sentinel-1 SAR dataset in Weining.

Sensor	Sentinel-1
Band	C
Acquisition orbit	Ascending
Incidence angle (°)	33.9
Swath width (km)	240
Repeat cycle (days)	12
Number of images	30
Ground resolution (m)	20
Temporal range	2 January 2018–28 December 2018

4. Methodology

Figure 2 illustrates a flowchart describing the methodology used in this study. The completion of this research mainly consisted of the following six steps:

(i) Collecting information on historical landslide and non-landslide points and establishing an evaluation index system based on landslide susceptibility.

(ii) Selecting landslide-influencing factors, obtaining corresponding datasets, and analyzing the relationships between these selected factors and landslides.

(iii) Preliminarily modeling landslide susceptibility using factors selected based on the RF model.

(iv) Evaluating the performance of the trained model and drawing dynamic LSMs with the model results.

(v) Performing an MT-InSAR analysis with the acquired Sentinel-1A dataset covering the study area and projecting the velocity in the line-of-sight (LOS) direction to the direction along the steepest slope through a geometric transformation process.

(vi) Using the MT-InSAR technology monitoring results to construct a correction matrix and refine the derived dynamic LSMs.

4.1. SMAP-R Data Preprocessing

Because the resolution of the acquired raw SMAP-R data was inconsistent with the resolution of interest, the kriging method was chosen for the interpolation preprocessing step, and the nearest-neighbor method was used to resample the interpolated data to a resolution of 30 m to ensure consistency with the data representing the other factors. According to the daily rainfall amounts recorded in the study area (provided by the local meteorological station) from 2017 to 2019 (Figure 3), the annual rainfall is mainly concentrated from May to October. Next, each year was divided into two dry seasons lasting from January to April and from January to December and one rainy season lasting from May to October, and the average soil moisture values in these two periods were obtained to represent the soil moisture in the corresponding seasons (Figure 4).

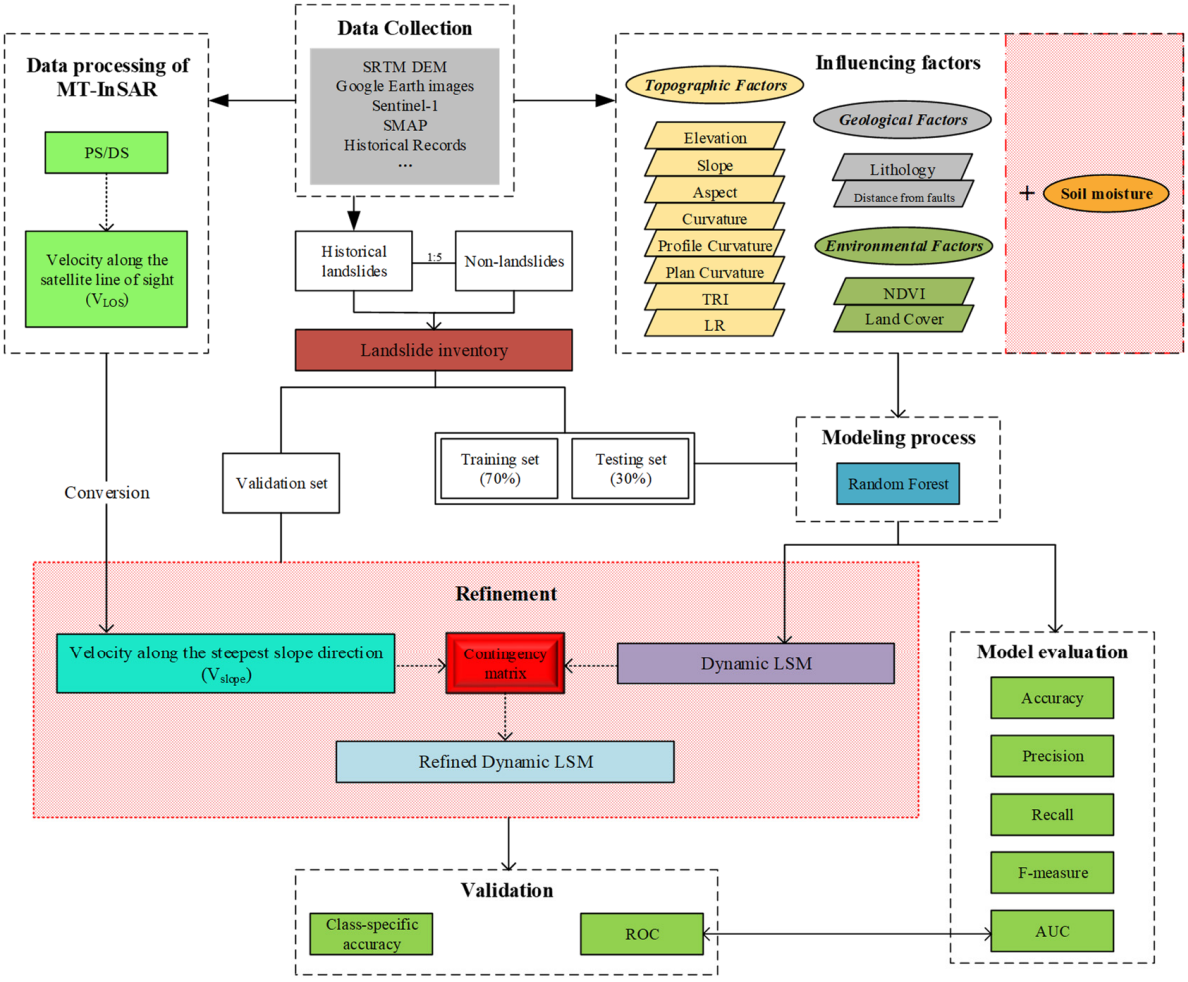

Figure 2. Flowchart of the methodology used in this study.

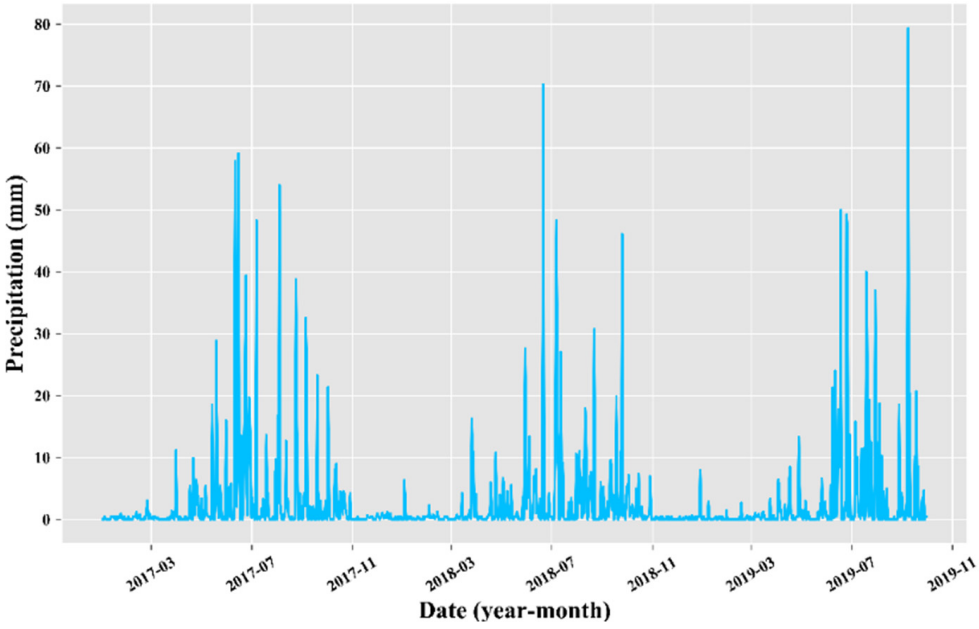

Figure 3. Daily precipitation totals in Weining from 2017 to 2019.

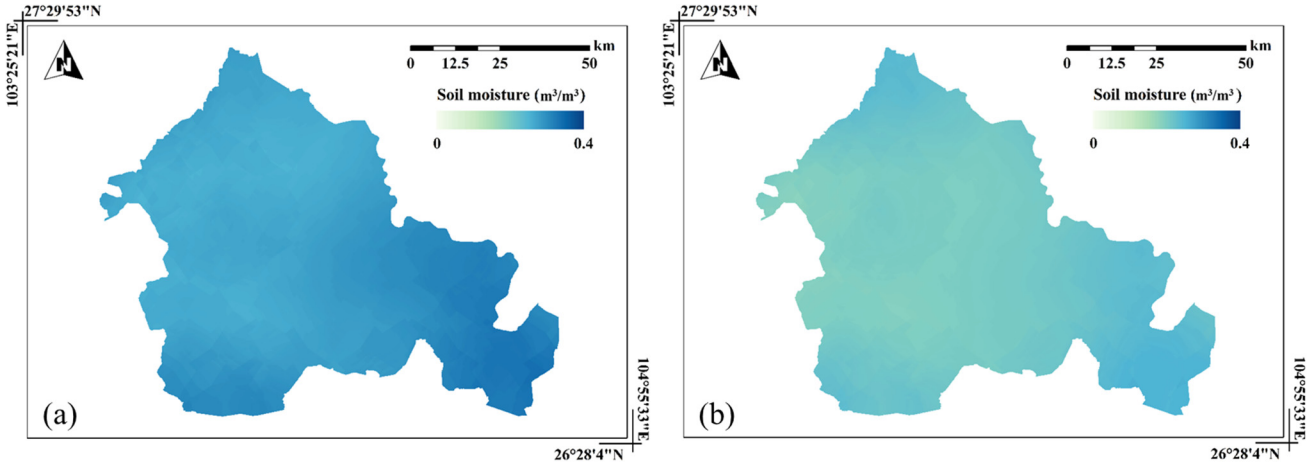

Figure 4. Map showing the average soil moisture in Weining from 2017 to 2019: (**a**) a map of the average soil moisture in the rainy season; and (**b**) a map of the average soil moisture in the dry season.

4.2. Preprocessing of Other Utilized Data

Considering the variety of data types, formats, and applications considered in this study, data preprocessing was necessary to meet the research needs.

Through the analysis and screening of the landslide inventory, landslides were divided into two groups: landslides that occurred before 2019 (historical landslides) were used for constructing LSM models and were divided into dry-season and rainy-season landslides according to the annual rainfall distribution. The newly added landslides from 2019 to 2020 (new landslides) were used for verification, as shown in Figure 5. At the same time, for the historical landslides, we selected 590 non-landslide points using a random sampling method at a ratio of 1:5 after performing many experiments using different ratios (e.g., 1:1, 1:5, and 1:10). Furthermore, both the historical landslide points and non-landslide points were randomly divided into a training set and a test set at a ratio of 7:3 to fit and test LSM models.

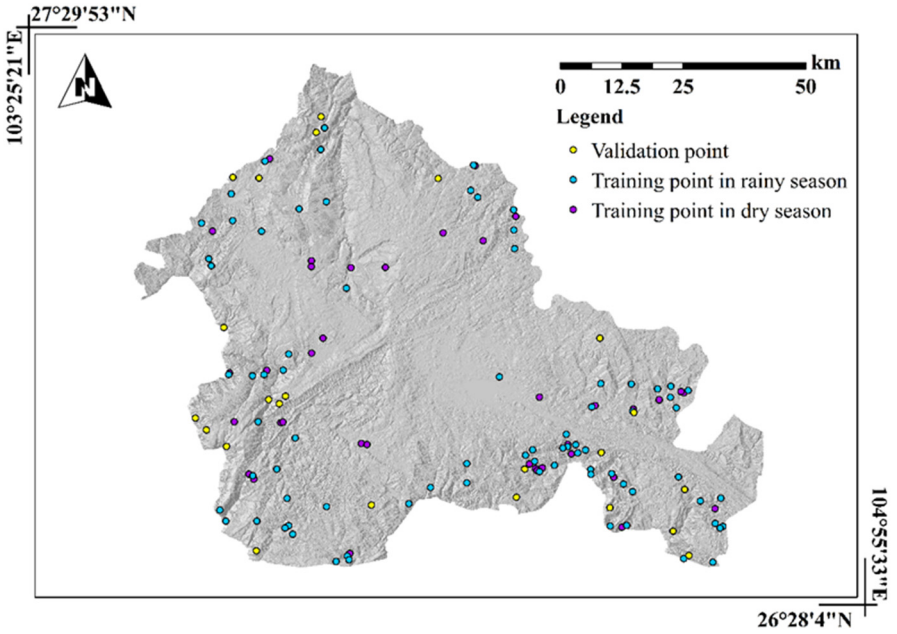

Figure 5. Landslide inventory map of Weining.

Regarding faults in Weining County, we established a multilevel buffer zone with an interval of 1000 m and a total extent of 5000 m to represent the range affected by faults.

The topographic factors (elevation, slope, aspect, curvature, plane curvature, profile curvature, TRI, and LR) were calculated using a 30-m DEM (derived from the NASA Space Shuttle Radar Terrain Mission (SRTM) Global 1-arc-second product). The following formulas were used to calculate the slope and TRI [46,47]:

$$\beta = \tan^{-1}(\text{rise}/\text{run}), \quad (1)$$

$$\text{TRI} = 1/\cos(\tan\beta * \pi/180) \quad (2)$$

where β refers to the slope gradient, rise is the elevation increment, and run is the increment in the horizontal direction.

After all impact factor thematic layers were projected to the same coordinate system, the data were resampled to a 30-m-resolution grid format, as shown in Figure 6.

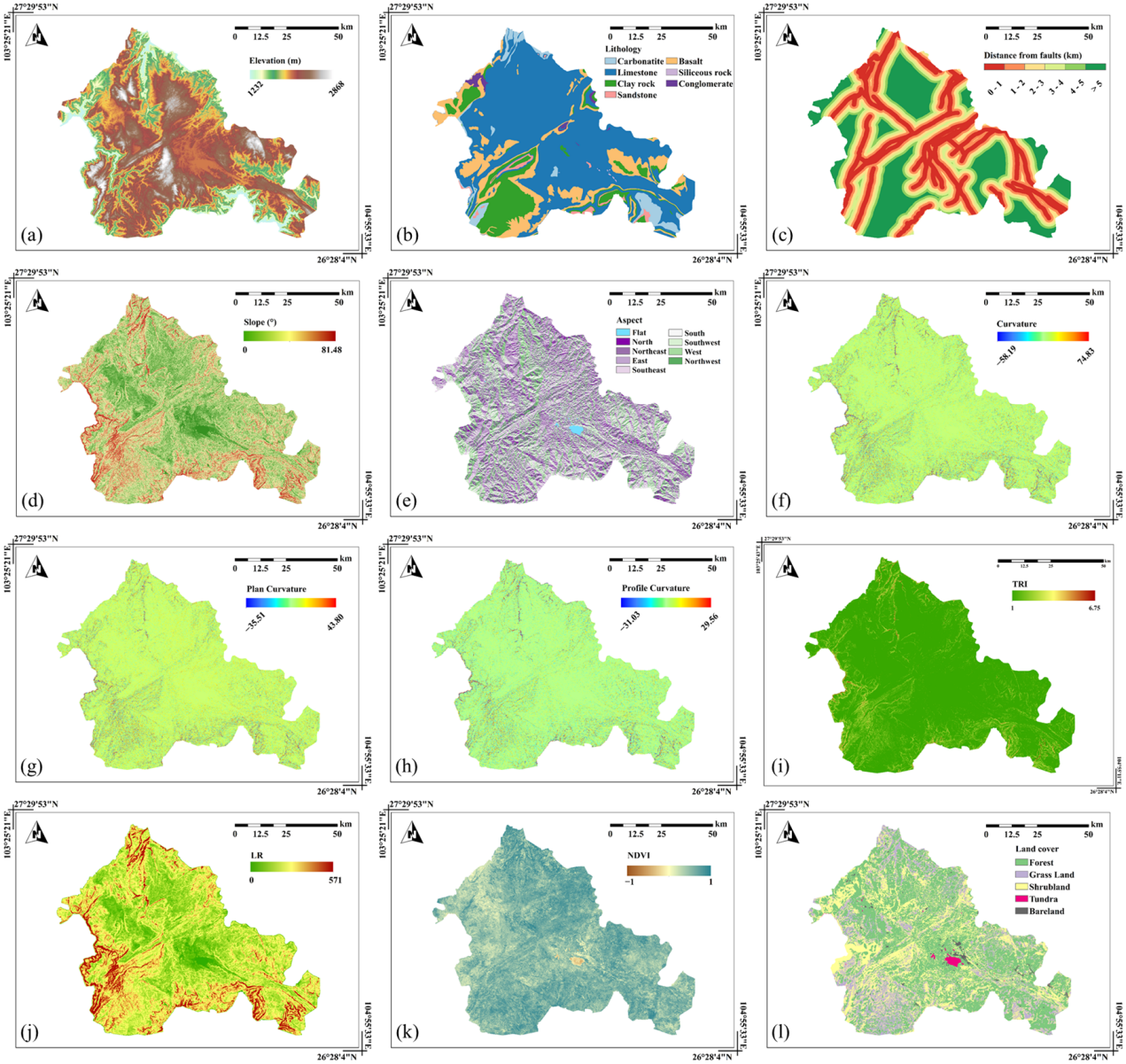

Figure 6. Layers representing landslide-influencing factors: (**a**) elevation; (**b**) lithology; (**c**) distance from faults; (**d**) slope; (**e**) aspect; (**f**) curvature; (**g**) plane curvature; (**h**) profile curvature; (**i**) TRI; (**j**) LR; (**k**) NDVI; and (**l**) land cover.

Then, the resampled impact factors were normalized to the [0,1] range to reduce the discreteness of the data. The utilized formula can be expressed as follows:

$$X^* = (X - X_{min})/(X_{max} - X_{min}) \quad (3)$$

4.3. Formatting of Mathematical Components

In this study, an RF model was implemented to generate the landslide susceptibility maps. As a machine learning algorithm, an RF is a method used to build multiple independent decision trees by random sampling and to combine these multiple decision trees for classification and prediction tasks. This method was first proposed by Breiman [55]. The main steps are shown in Figure 7. First, n new sample sets were randomly selected from the original training dataset through replacement using the bootstrap method, and n decision trees were constructed. Furthermore, a group of features was randomly selected during each resampling step, and n decision trees were constructed on this basis. Finally, the generated trees were combined into an RF that was used to classify the new data, and the classification result was determined by decision tree voting. The RF model is not only very resistant to overfitting when dealing with complex data but is also very accomplished when addressing the problems of default values and noise; that is, the RF model shows strong robustness and accuracy in the face of high-dimensional data [56].

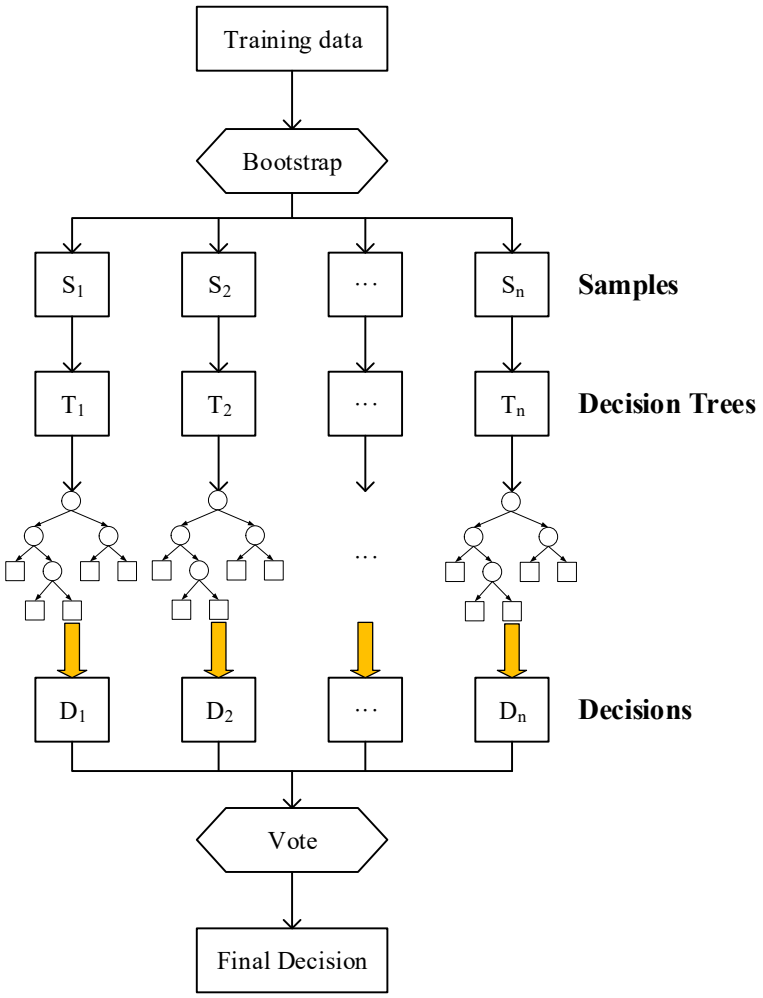

Figure 7. Schematic diagram of the RF modeling process.

During the modeling process, the landslide samples were assigned a value of 1, while the non-landslide samples were assigned a value of 0. Considering the possible advantages and limitations of different mapping unit scales and types in landslide susceptibility

mapping research [57], as well as the calculation accuracy and feasibility, grid cells were selected as the mapping units in this study.

Landslide susceptibility mapping is a method that can effectively reflect the risk of landslides in an area. Based on the 13 factors listed above, in this study, we generated LSMs at an evaluation unit resolution of 30 × 30 m with and without SMAP-R. Next, these LSMs were reclassified into the following four categories using the Jenks natural breakpoint grading method: (i) low to zero susceptibility; (ii) moderate susceptibility; (iii) high susceptibility; and (iv) very high susceptibility.

4.4. MT-InSAR

In this paper, we first implement the basic D-InSAR processing steps, including the image preprocessing and single-look complex (SLC) image registration steps. After acquiring registered SLC images, interferogram pairs were selected to form an interferogram network in terms of nonrepetitive spatiotemporal baselines. During this process, an interferogram stack was obtained with a maximum temporal baseline of 36 days and a maximum spatial baseline of 177.1 m. Moreover, the terrain-dependent phase was removed using a DEM. Within the interferogram stack obtained in the previous step, appropriate persistent scatterer (PS) candidate points were selected depending on the amplitude discrete index and the spectral properties of the SLCs. In addition, we employed the two-sample Anderson-Darling (AD) test to determine statistically homogenous pixels (SHPs); SHPs greater than 20 were considered distributed scatterer (DS) candidates. Furthermore, the phase before the DS detection step was optimized via the coherent weighted phase connection method. The selected pixels were connected in pairs to form a point network, and the differential phase of each edge and interferogram in the M pairs were calculated. In particular, the phase discrepancy of each edge in the network was obtained by distinguishing the phases of two pixels. The periodogram estimation method and the weighted least squares phase unwrapping method were used to estimate and solve the differential deformation rate and terrain differential error on each edge, respectively. These differential values were then integrated into the selected pixel set. The residual phase, including the nonlinear deformation phase, atmospheric phase, and noise information, was derived by subtracting the above differential value from the initial differential interferograms. Temporal and spatial filtering steps were applied to separate the atmospheric and nonlinear deformation phases, relying on their unique temporal and spatial distribution characteristics. Finally, the deformation information in the time series of each PS/ DS point was inverted using the clean phase derived in the previous step.

Each PS/DS point represents a one-dimensional projection in the direction of the satellite LOS rather than the real deformation that occurs in three-dimensional space [58]. To represent the deformation in a way that is more suitable for depicting the actual situation, a postprocessing step was required. We referenced the method proposed by Bianchini [59] and Notti [60], in which a DEM (from which the slope and aspect information can be derived) and satellite parameters (the LOS azimuth, incident angle, and direction cosine) are combined to reproject the deformation rates of all PS/DS values measured along the LOS direction (V_{LOS}) to a new rate along the steepest-slope direction (V_{slope}), which is considered a potential slope failure correlation representing the most likely actual direction of motion [61,62]. This method is useful when the applied SAR images are acquired by different satellite sensors (with different LOSs) and/or different orbits (ascending and descending). Finally, the PS/DS points with slopes less than five degrees or positive displacement rates were eliminated to map the integrated displacement results.

4.5. Refinement

MT-InSAR technology is capable of monitoring and identifying slope instability, but the corresponding signs may occur in places that are hard to reach or where the displacement is small, slow, or otherwise difficult to detect. In other words, displacement may not be recorded properly by traditional geological surveys. In addition, the MT-InSAR

dataset can also reflect the dynamic deformation process of unstable slopes with the regular production of SAR data. Therefore, combining surface deformation information with a LSM can increase the susceptibility of slope units to surface displacement phenomena, reduce the number of underreported risks as much as possible, and ameliorate the timeliness and applicability of the utilized LSM. In contrast, slope units in cells that are considered stable in the MT-InSAR measurements retain their original susceptibility levels in the resulting LSM.

We merged the LSM along the steepest-slope direction (V_{slope}) at the scale of each evaluation unit using a correction matrix. First, we reclassified the previously obtained V_{slope} into four categories based on the standard deviation (σ = 8 mm/year). The higher the displacement rate was, the higher the level was: (i) low-speed deformation ($0 \leq V_{slope} \leq 8$ mm/year), (ii) medium-speed deformation ($8 < V_{slope} \leq 16$ mm/year), (iii) high-speed deformation ($16 < V_{slope} \leq 24$ mm/year), and (iv) ultrahigh-speed deformation (24 mm/year $< V_{slope}$). Next, by combining the initial dynamic LSM obtained by the RF, we were able to perform susceptibility refinements according to a matrix (Table 3) in which the number of corrections was enumerated for each possible case. For each evaluation unit, we determined the corresponding correction number based on the speed interval associated with the average V_{slope} value obtained for at least four surrounding PS/DS points, potentially ensuring the stability of the susceptibility or increasing it from degree 1 to degree 4. For example, for an evaluation unit with an original susceptibility degree of 2, if the average V_{slope} value of the four surrounding pixels is within the $16 < V_{slope} \leq 24$ mm/year interval, then the corrected value of the unit is +1, and the corrected susceptibility degree is 3. The faster the displacement rate is, the larger the correction value and the higher the correction level. Notably, the susceptibility of each cell is not adjusted if fewer than four PS/DS points are located around the cell or if the raw susceptibility level is the highest (degree 4).

Table 3. Correction matrix applied to the LSMs considering the average V_{slope} values.

		V_{slope} (mm/year)			
	Class	**0–8**	**8–16**	**16–24**	**>24**
Degree of susceptibility	1	0	+1	+2	+3
	2	0	0	+1	+2
	3	0	0	0	+1
	4	0	0	0	0

4.6. Validation

Unless the performance and accuracy of a model are confirmed, no matter which model is used to generate LSMs, the results are of no practical significance [63]. Therefore, validating the LSM was an integral part of this study. Here, we used two kinds of methods to perform this validation, as described below.

4.6.1. Class-Specific Accuracy Validation

In an effort to verify the correlation between the landslide inventory and the LSM, in this study we applied a relative landslide density index (degree of fitting) that considered landslides in areas of different susceptibilities and the total number of units in each area to evaluate the model fit. The fit (DF_i) of the LSM can be calculated as follows [64]:

$$DF_i = 100 \cdot \frac{n_i/N_i}{\sum n_i/N_i} \quad (4)$$

where n_i is the number of units occupied by landslides on the current susceptibility map, N_i represents the number of units covered by the susceptibility class i, and DF_i stands for the percentage of landslides in the susceptibility class i with regards to the number of units in the area. The larger the DF_i value, the larger the range of landslides occurring in the

susceptibility class i is, and the higher the accuracy of the landslide prediction results for this class is.

4.6.2. Statistical Validation

In this study, the susceptibility degree is regarded as a binary classifier denoting the possible or unlikely occurrence of landslides in the corresponding area. Based on this assumption, we analyzed the landslide susceptibility evaluation results by constructing an ROC curve.

A ROC curve is a visualization technique based on the evaluation and selection of the classifier's performance. This technique has a long history of application in signal detection theory and has been used to represent the trade-off between the classifier hit rate and false alarm rate [65]. The ROC curve is constructed using a confusion matrix and two metrics (sensitivity and specificity) [66]. Since both a classifier and an instance were provided in this study, a 2×2 confusion matrix could be constructed with four possible outcomes: if an instance is true (T) and classified as positive (P), it is counted as a true positive (TP); if a true instance was classified as negative (N), it was counted as a false negative (FN); if an instance was false (F) and was classified as negative (N), it was counted as a true negative (TN); and if an F was classified as positive (P), it was counted as a false positive (FP). The confusion matrix and equations for several common metrics that can be calculated from the matrix are shown in Figure 8. The TP rate (also called the model sensitivity, hit rate, or recall rate) of a classifier can be expressed as follows:

$$\text{TP rate} = {}^{\text{TP}}/_{\text{TP} + \text{FN}} \quad (5)$$

The FP rate (or false hit rate) of a classifier can be estimated using the following equation:

$$\text{FP rate} = {}^{\text{FP}}/_{\text{TN} + \text{FP}} \quad (6)$$

The TN rate (specificity) can be calculated as follows:

$$\text{TN rate} = {}^{\text{TN}}/_{(\text{FP} + \text{TN})} = 1 - \text{FP rate} \quad (7)$$

where TP refers to a category that is correctly identified as positive in the actual true sample, FP represents the category that is actually false but was incorrectly identified as positive.

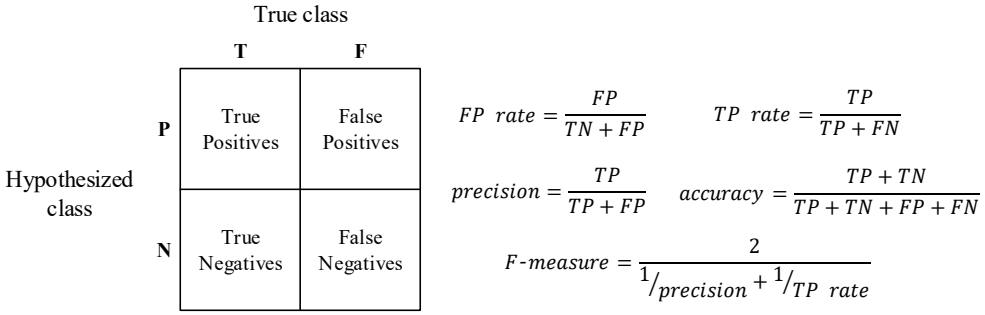

Figure 8. Schematic diagram of the RF modeling process.

Figure 8 shows the confusion matrix and the formulas for several common metrics. The values on the main diagonal represent correct decisions, while the values on the secondary diagonal represent errors (or confusion) between classes. Calculating the AUC is a currently accepted metric for evaluating and comparing classifiers [67]. The purpose of the AUC is to reduce the ROC curve to a single scalar value that represents the expected performance. Since AUC is a part of the area of a unit square, its value is always between 0 and 1. Random predictions provide a diagonal line from the bottom left to the top right; thus, the AUC obtained for any valid binary classifier should be greater than or equal to 0.5.

5. Results

5.1. Dynamic LSM (D-LSM)

An LSM of Weining County was generated by the trained RF model. This mapping process was equivalent to visualizing the landslide probability of each grid predicted by the model in the study area. The models were also evaluated using ROCs derived based on statistical methods. Next, we obtained the LSM (Figure 9a,c,e) after classifying the susceptibility into 4 categories using the Jenks natural breakpoint grading method and a user-defined method. Figure 9a shows the LSM (Traditional LSM, T-LSM) generated using 12 factors among the 13 factors, excluding soil moisture, and 31.5672% of the area had zero to low susceptibility, 25.1954% was characterized by medium susceptibility, 22.1211% had high susceptibility, and 21.1163% had very high susceptibility. Figure 9c shows the dynamic LSM generated by setting May to October as the time period of interest (the rainy-season D-LSM); this process involved 13 factors, including the average soil moisture during the rainy season. The results show that low-, medium-, high-, and very-high-susceptibility regions accounted for 32.3319%, 26.3491%, 23.8692%, and 17.4498% of the total study area, respectively. In contrast, the D-LSM shown in Figure 9e focused on the periods from January to April and from November to December (the dry-season D-LSM); to obtain this LSM, the average dry-season soil moisture value was used to represent the soil moisture factor. Here, the low-, medium-, high-, and very-high-susceptibility regions accounted for 35.3609%, 29.1598%, 27.8972%, and 7.58213% of the overall study area, respectively (Table 4).

Table 4. Overview of the T-LSM and D-LSM results.

Degree of Susceptibility	T-LSM		Dry-Season D-LSM		Rainy-Season D-LSM	
	No. of Cells	%	No. of Cells	%	No. of Cells	%
1	2,292,211	31.5672	2,567,685	35.3609	2,347,737	32.3319
2	1,829,534	25.1954	2,117,406	29.1598	1,913,308	26.3491
3	1,606,298	22.1211	2,025,717	27.8972	1,733,234	23.8692
4	1,533,332	21.1163	550,567	7.58213	1,267,096	17.4498

Figure 9b,d show the ROC curves of Figure 9a,c on their left sides. Tables 5 and 6 list the statistical results of the accuracy, precision, recall, and F-measure values obtained by the T-LSM and rainy-season D-LSM models, respectively, using the training and test datasets. By analyzing the performance of these datasets, this result indicates that this model has quite good predictive capabilities. We can conclude that the AUC value, accuracy, precision, recall, and F-measure values obtained by the model when adopting traditional impact factors were 0.8986, 0.7588, 0.3955, 0.8968, and 0.5502, respectively. In addition, for the model in which rainy-season soil moisture was considered, these five indices were equal to 0.9132, 0.7937, 0.4362, 0.9063, and 0.5860, respectively; obviously, the latter model had a better prediction effect than the first model, with respective index differences of 0.0146, 0.0349, 0.0407, 0.0095, and 0.0358.

Table 5. Performance of the T-LSM prediction model.

Dataset	Statistical Validation	Value
Training	accuracy	0.8003
	precision	0.4313
	recall	0.9232
	F-measure	0.5958
Testing	accuracy	0.7588
	precision	0.3955
	recall	0.8968
	F-measure	0.5502

Table 6. Performance of the rainy-season D-LSM prediction model.

Dataset	Statistical Validation	Value
Training	accuracy	0.8203
	precision	0.4634
	recall	0.9210
	F-measure	0.6172
Testing	accuracy	0.7937
	precision	0.4362
	recall	0.9063
	F-measure	0.5860

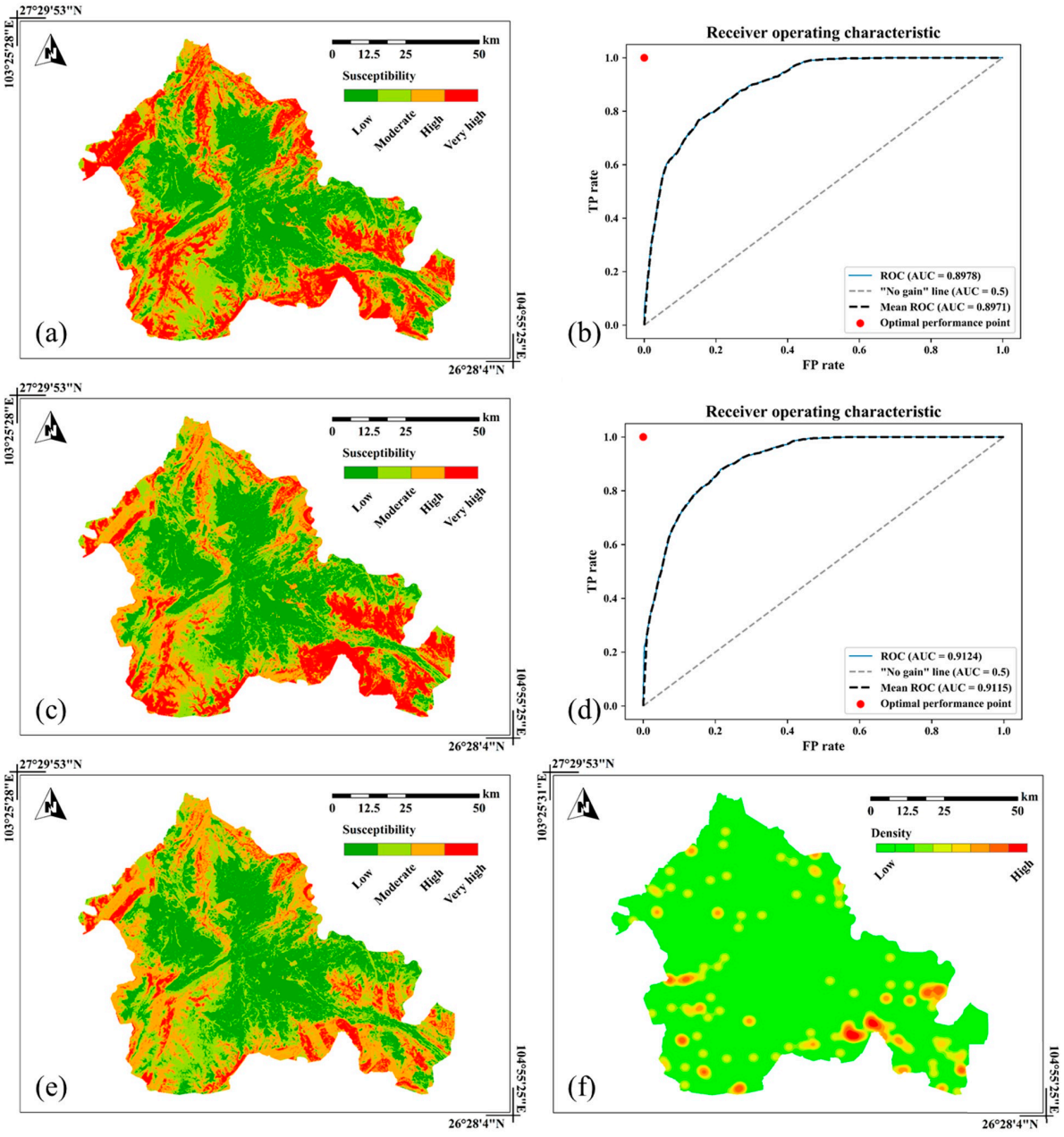

Figure 9. LSMs and actual landslide density maps: (**a**) the T-LSM; (**b**) ROC curve and AUC result of the T-LSM with testing dataset; (**c**) rainy-season D-LSM; (**d**) ROC curve and AUC result of the rainy-season D-LSM with testing dataset; (**e**) dry-season D-LSM; and (**f**) actual landslide density map.

Visually, the LSMs created by the three utilized datasets were very similar. The high- and very-high-risk areas were mainly distributed in the southwestern and southeastern parts of the study area, except for small areas in the northwestern and northeastern regions. Moreover, comparing these three LSMs with the density distribution map of historical landslides (Figure 9f), it is clear that the landslide distribution is generally consistent with the landslide susceptibility. However, by comparing Figure 9a,b,e, the D-LSM was found to be dynamic following the introduction of soil moisture. In particular, the very-high-susceptibility areas in the western and northern regions were significantly reduced in area. In fact, these areas have experienced relatively few historical landslides. Simply put, the overestimation of landslide susceptibility by traditional factors in these regions was attenuated by the soil moisture conditions.

To better reflect the role of dynamic soil moisture properties in the evaluation of local landslide susceptibility, we used quantitative analysis methods to quantify the susceptibility based on the qualitative evaluation of LSMs in the study area.

The differences between the T-LSM and the two D-LSMs were first evaluated by computing each unit based on susceptibility. The statistical results are shown in Table 7. For the dry-season D-LSM (Figure 10a), the susceptibility degrees of 628 units decreased by 2 degrees, those of 1,847,216 units decreased by 1 degree, and those of 26,887 units increased by 1 degree. For the rainy-season D-LSM (Figure 10b), the susceptibility degrees of 985 units decreased by 2 degrees, those of 1,010,667 units decreased by 1 degree, those of 551,571 units increased by 1 degree, and those of 2 units increased by 2 degrees. The discrepancies between the two D-LSMs (Figure 10c) showed that the susceptibility of 56,436 units decreased by 1 degree, that of 1,374,533 units increased by 1 degree, and that of 21,213 units increased by 2 degrees.

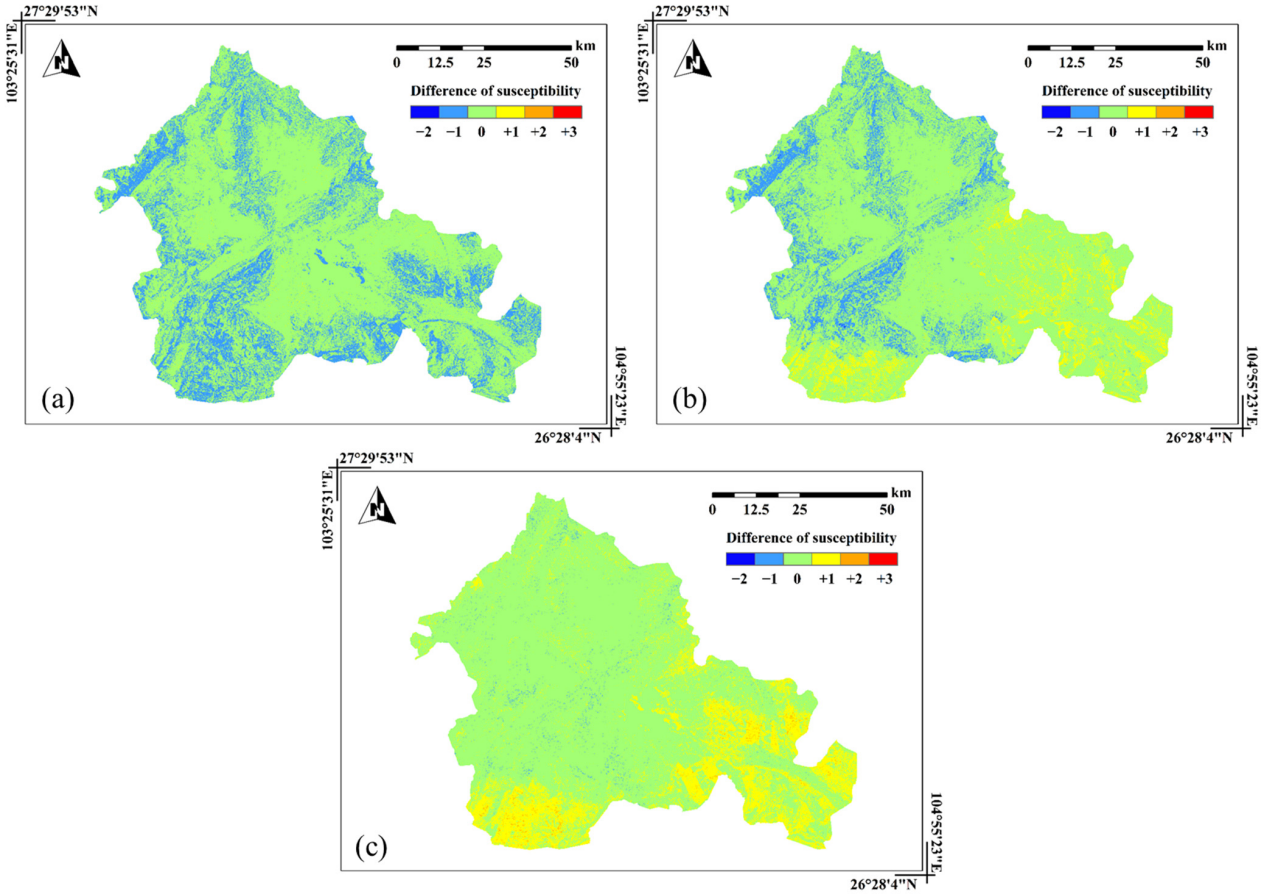

Figure 10. Maps showing the differences between the derived LSMs: (**a**) the T-LSM and the dry-season D-LSM; (**b**) the T-LSM and the rainy-season D-LSM; and (**c**) the rainy-season and dry-season D-LSMs.

Table 7. Overview of the differences between the T-LSM and D-LSMs.

Difference in the Susceptibility Degree	Difference between the T-LSM and Dry-Season D-LSM		Difference between the T-LSM and Rainy-Season D-LSM		Difference between the Dry-Season and Rainy-Season D-LSMs	
	No. of Cells	%	No. of Cells	%	No. of Cells	%
−2	628	0.0087	985	0.0136		
−1	1,847,216	25.4389	1,010,667	13.9184	56,436	0.7772
0	5,386,644	74.1822	5,698,150	78.4721	5,809,193	80.0013
+1	26,887	0.3703	551,571	7.5960	1,374,533	18.9294
+2			2	0.00003	21,213	0.2921

Statistically, we compared and analyzed the density distributions of historical landslides in the dry (Figure 11a) and rainy (Figure 11b) seasons with the above three LSMs (Figure 11c,d). Through this comparison, we confirmed that the density of corresponding landslides increased gradually as the susceptibility reflected in the D-LSM increased in both the dry and rainy seasons. In particular, the landslide density of the D-LSM was significantly higher than that of the T-LSM in the high- and very-high-susceptibility regions.

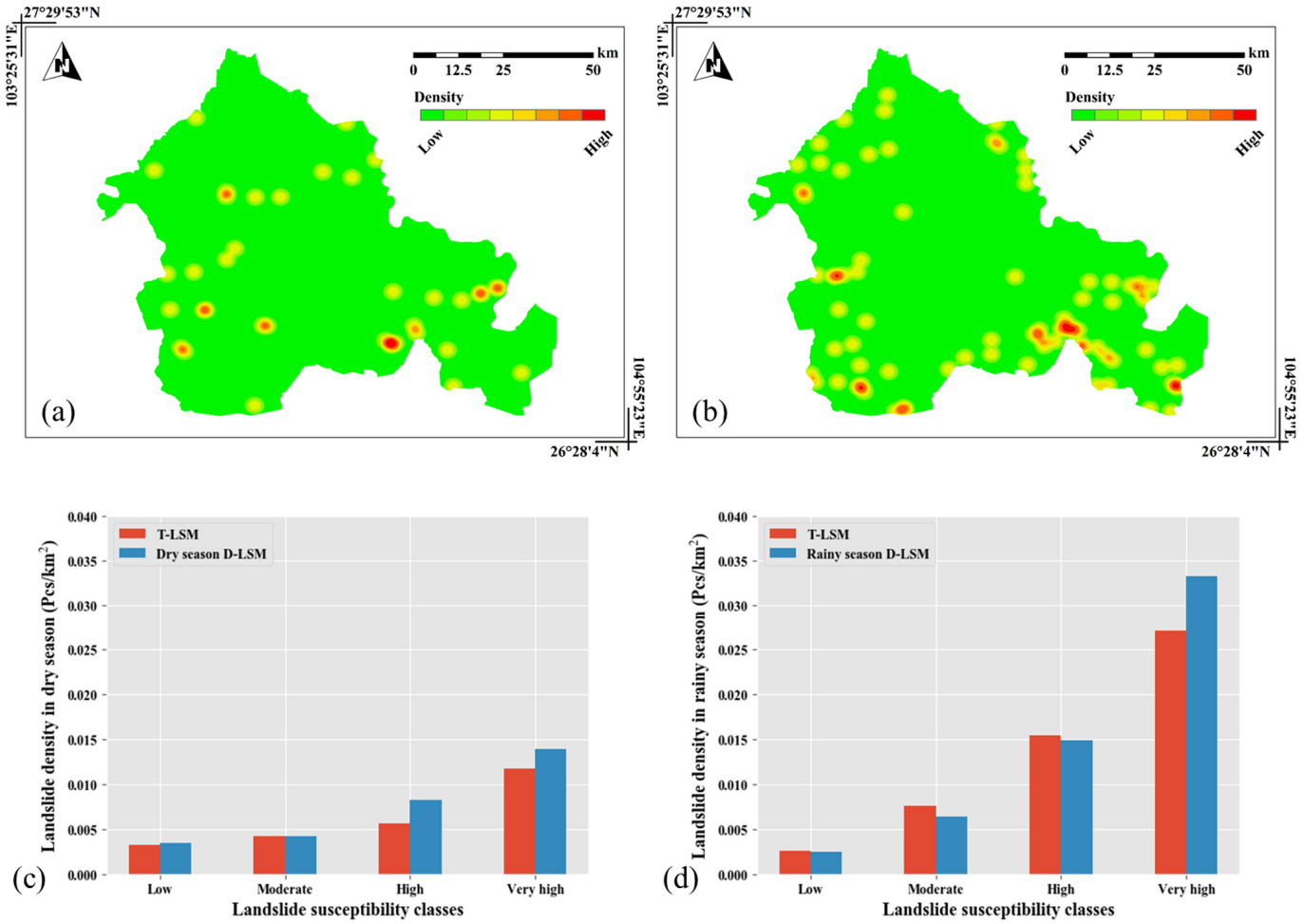

Figure 11. Maps of historical landslide densities and statistical landslide susceptibility diagrams: (**a**) the dry-season landslide density map; (**b**) the rainy-season landslide density map; (**c**) the landslide density in each susceptibility level between the T-LSM and D-LSM in the dry season; and (**d**) the landslide density in each susceptibility level between the T-LSM and D-LSM in the rainy season.

Next, we evaluated the validity of the derived susceptibility maps by comparing the predicted LSMs with the landslide inventory, which contained both a historical landslide dataset for training and a new landslide dataset for validation. Due to the small number of samples contained in the latter dataset, it was considered a whole dataset on its own and was not divided into the dry- and rainy-season datasets to ensure the reliability of the statistical results to the greatest possible extent. Under this premise, the most direct source of susceptibility was the rainy-season D-LSM. Therefore, only the landslide fitting degrees of the T-LSM and rainy-season D-LSM were tested in this work. The fitting degrees calculated using the historical landslides recorded in the dry and rainy seasons (Figure 12a,b) show that landslides were mostly concentrated in high-susceptibility areas. Compared to the T-LSM, the D-LSM showed that the proportions of landslide units in the low- and moderate-susceptibility classes were small, while the proportion of landslides in the very-high-susceptibility region was relatively large. Similarly, the fitting degree results derived using the validation landslide dataset (Figure 12c) showed that landslides were again concentrated in the high-susceptibility region. Comparing the very-high-susceptibility regions in the T-LSM and D-LSM, the latter has a smaller proportion of landslide units corresponding to low and medium susceptibility, while the former has a larger proportion of landslides in the very-high-susceptibility region. At present, a large number of landslides have been clearly distributed in areas of high and very high susceptibility, especially those areas derived after the introduction of the soil moisture factor; in simple terms, this factor improved the accuracy of the landslide prediction work in the study area and exerted a certain optimization effect on the resulting LSM.

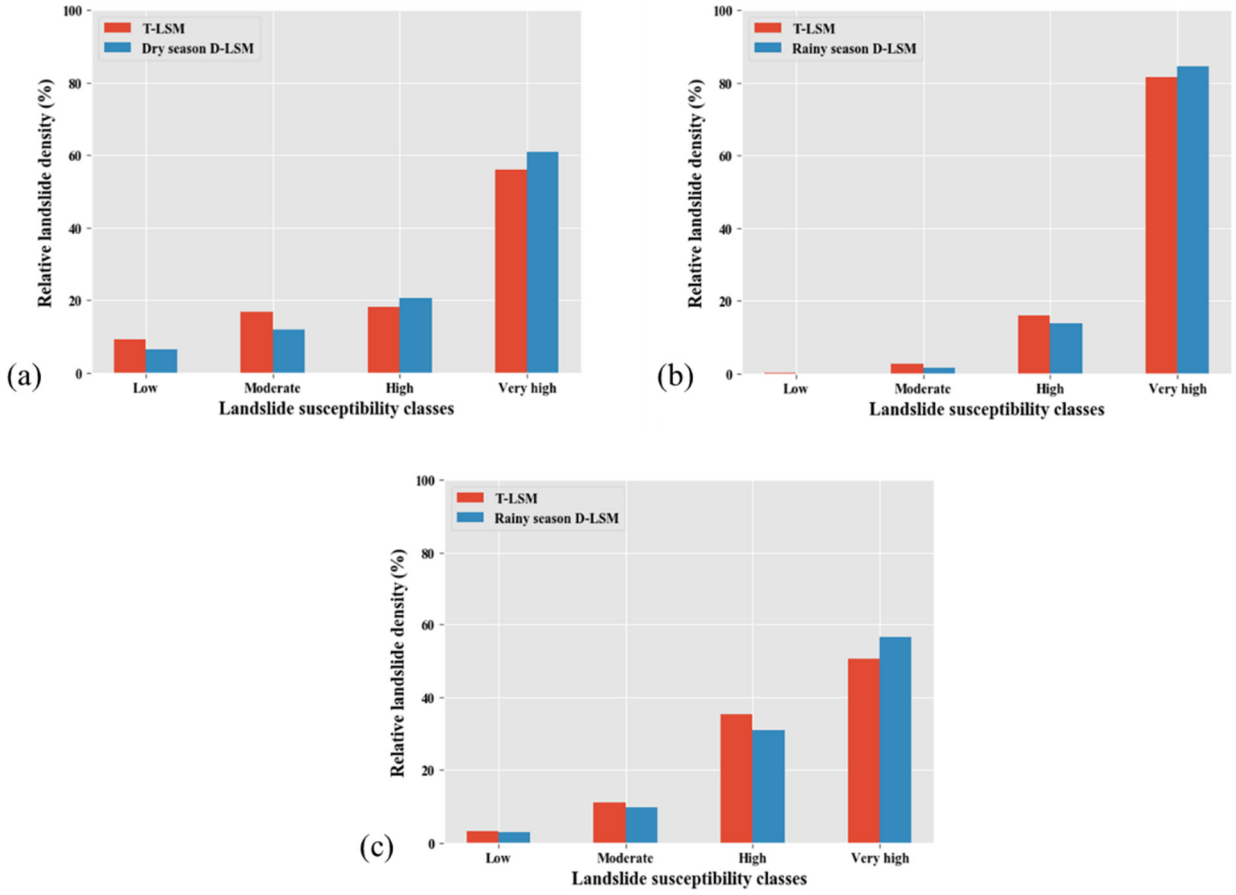

Figure 12. Relative landslide density index values of the derived LSMs: (**a**) relative historical landslide density index values of the T-LSM and D-LSM in the dry season; (**b**) relative historical landslide density index values of the T-LSM and D-LSM in the rainy season; and (**c**) relative new landslide density index values of the T-LSM and D-LSM in the rainy season.

5.2. MT-InSAR

MT-InSAR analysis was performed on the whole territory of Weining County using the Sentinel-1A dataset. In total, 47,677,026 PS/DS points were extracted at a density of 7570 points/km^2. At each point, the annual average deformation rate, historical deformation information, and 3D position information were recorded. The deformation rate was determined by obtaining the average PS/DS displacement velocity over the time range covered by the interferogram in mm/year. Through a brief visual interpretation of the velocity map along the LOS direction (Figure 13a), we found that obvious deformation occurred on the surface. A negative deformation value in the figure indicates that the point was located far from the radar along the LOS direction, while a positive deformation value suggests proximity to the radar. Especially in the western part of the study area, the maximum absolute velocity (V_{LOS}) reaches a value of approximately 143 mm/year. Figure 13b shows the velocity along the direction of the steepest slope (V_{slope}). In this figure, the maximum absolute rate reaches approximately 250 mm/year. Since PS/DSs located in flat areas and in areas in which the displacement velocity is greater than 0 were discarded, the point density in the V_{slope} map is significantly lower than that in the V_{LOS} map. To ensure that the standard deviation of the MT-InSAR dataset was reasonable, we considered PS/DSs corresponding to absolute V_{LOS} values in the 0–8 mm/year interval as stable. Under this assumption, a total of approximately 96% of the points in the study area were considered stable. Of course, in the real situation, some unstable PS/DSs exist in the obtained ground deformation velocity map, causing the map to not always correspond to the real landslide distribution.

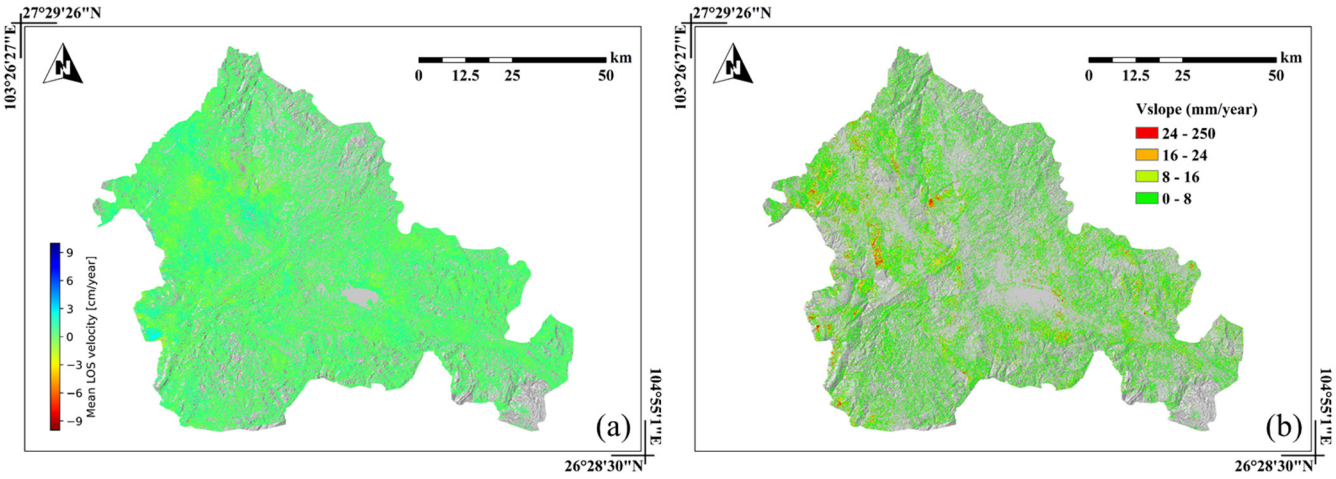

Figure 13. Ground deformation velocity maps: (**a**) ground deformation velocity maps along the satellite LOS and (**b**) ground deformation velocity maps along the steepest-slope direction.

5.3. Refined D-LSM (D-RLSM)

The Refined LSM (RLSM) was obtained based on the acquired D-LSM and the surface deformation magnitudes measured by MT-InSAR technology. The first step in this process was the resampling of the V_{slope} value of each PS/DS to each cell (30 × 30 m); at this point, V_{slope} was no longer related to a single PS/DS point but to a 30 × 30 m unit. After creating a new velocity map (Figure 13b), the correction matrix was able to improve the previously obtained D-LSM. Under the circumstances that the time period of the SAR data selected in this study covered the whole year of 2018, the most direct source of RLSM susceptibility was the rainy-season D-LSM. Therefore, in this work, we only modified the T-LSM and the rainy-season D-LSM. The final RLSM is shown in Figure 14. Figure 14a shows the correction results obtained based on the T-LSM (T-RLSM), in which 30.6992% of the area had low susceptibility, 25.5569% had medium susceptibility, 22.2201% had high susceptibility, and 21.5237% had very high susceptibility. Figure 14b provides the RLSM obtained by updating the D-LSM (D-RLSM). The statistical analysis revealed that the low-, medium-, high-, and

very-high-susceptibility regions composed 31.4236%, 26.7181%, 23.9557%, and 17.9025% of the study area, respectively (Table 8).

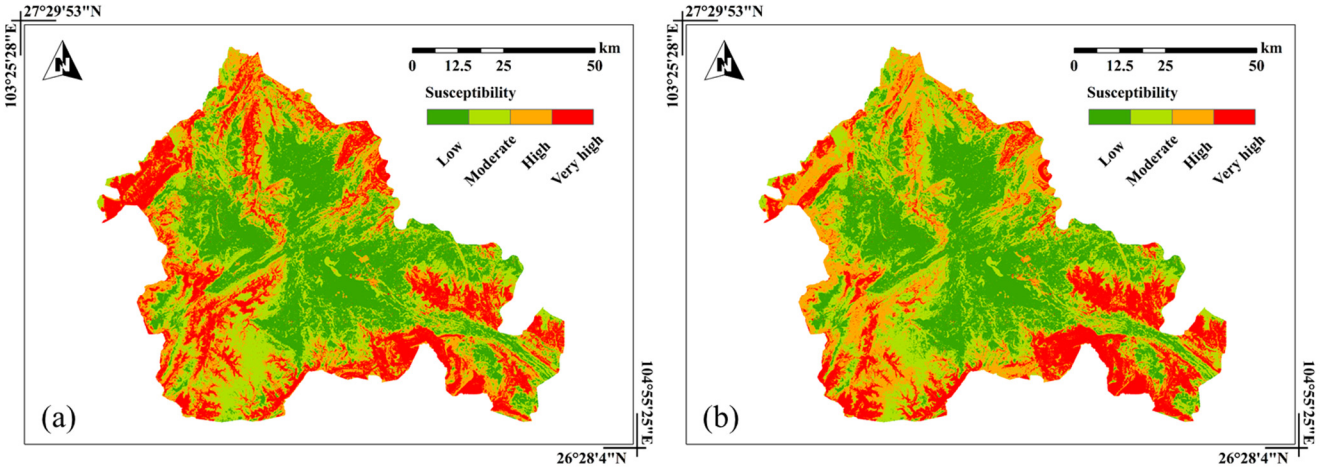

Figure 14. RLSM results: (**a**) the T-RLSM and (**b**) the D-RLSM.

Table 8. Overview of the derived RLSMs.

Degree of Susceptibility	T-RLSM		Rainy-Season D-RLSM	
	No. of Cells	%	No. of Cells	%
1	2,229,187	30.6992	2,281,785	31.4236
2	1,855,782	25.5569	1,940,105	26.7181
3	1,613,486	22.2201	1,739,516	23.9557
4	1,562,920	21.5237	1,299,969	17.9025

Overall, the susceptibility distributions of the T- and D-RLSMs and their corresponding LSMs obtained before refinement were basically consistent. In detail, the area percentages of low-susceptibility regions in the study area were reduced by 0.868% and 0.9083% in the T- and D-RLSMs, respectively. The area percentages of the other three susceptibility classes all saw small increases, especially the very-high-susceptibility class, which increased by 0.4074% and 0.4527% in the T- and D-RLSMs, respectively. From this result, we can infer that the surface deformation rate can be used to update the LSM in the study area to improve timeliness, providing a certain degree of practicability.

To evaluate the inconsistencies in the derived LSMs, we calculated the differences within the four pairs of combinations in the above LSMs/RLSMs separately according to the susceptibility class of each evaluation unit (Figure 15): (i) the T-LSM and T-RLSM; (ii) the D-LSM and D-RLSM; (iii) the D-RLSM and T-LSM; and (iv) the T-RLSM and D-RLSM. The differences derived for combinations (i) and (ii) are shown in Figure 15a and b, respectively. Initially, the figures show that the regional distributions of the susceptibility degrees are very similar between the two groups and are consistent with the corresponding positions of high V_{slope} values. Concentrating on the northwestern and entire southern regions, the statistical analysis (Table 9) indicated that only 1.2365% and 1.3244% of the cells changed, respectively, among which approximately two-thirds of the cells underwent 1-degree susceptibility increases. Figure 15c provides a visualization of the discrepancies derived for combination (iii). The statistical information (Table 10) shows that most cells in the T-LSM remained consistent when the soil moisture and MT-InSAR deformation information were integrated. However, 22.4914% of the cells underwent susceptibility changes, corresponding to an area of approximately 1416.5 km^2. Among these cells, the susceptibility degrees of 972 units decreased by 2, those of 996,480 units decreased by 1 degree, those of 606,255 cells increased by 1 degree, those of 19,356 units increased by 2 degrees, and those of 10,125 units increased by 3 degrees. Furthermore, the differences between the two images (Figure 15d)

assessed in combination (iv) indicate a decrease in the susceptibility degree similar to that seen in combination (iii). While 89,784 more cells maintained the same susceptibility degree in this combination, the number of cells that underwent susceptibility increases of 1 degree decreased by 60,305, while 2 more cells underwent susceptibility degree increases of 2.

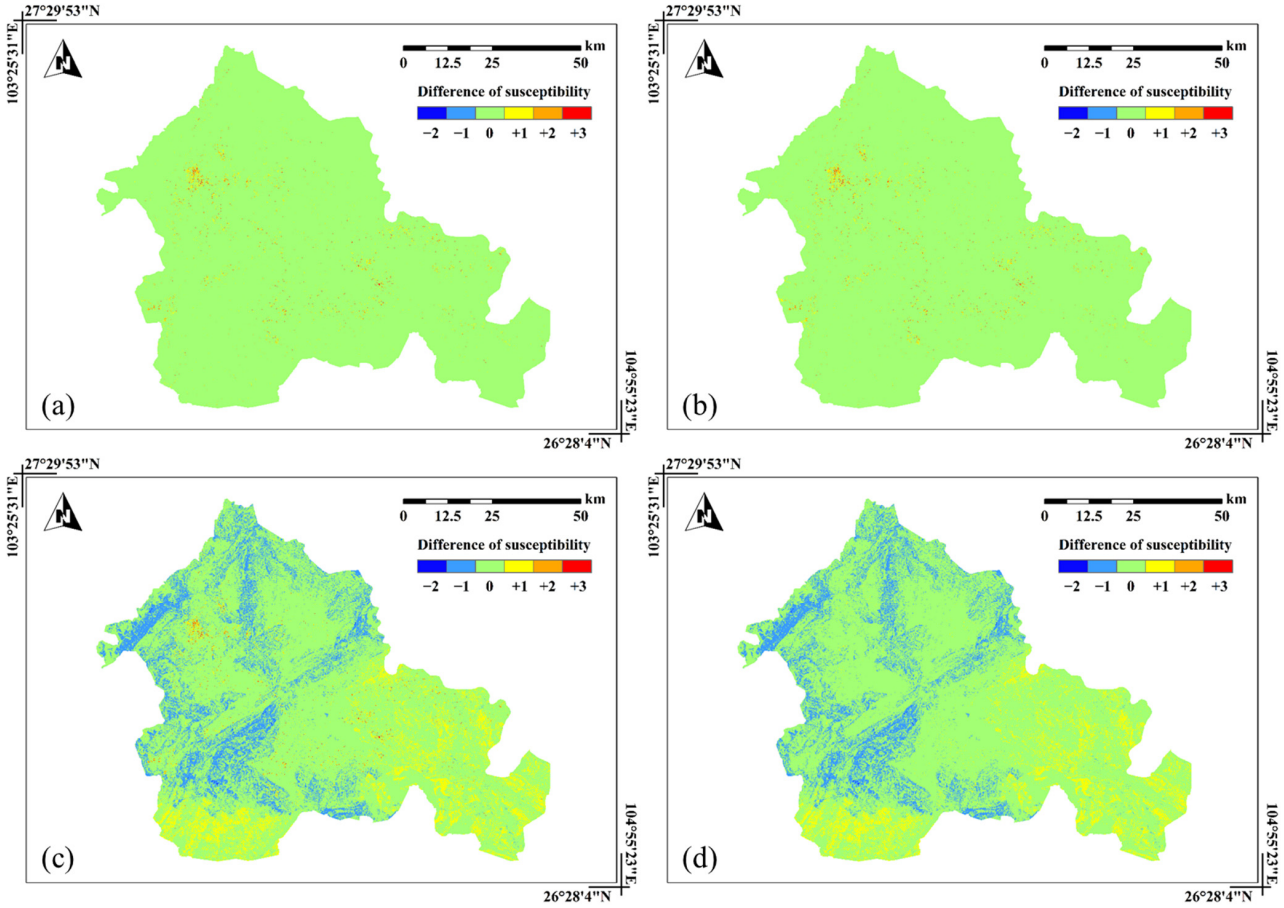

Figure 15. Maps displaying the differences between the derived LSMs and RLSMs: (**a**) the T-LSM and T-RLSM; (**b**) the D-LSM and D-RLSM; (**c**) the D-RLSM and T-LSM; and (**d**) the T-RLSM and D-RLSM.

Table 9. Overview of the differences between the LSMs derived before and after refinement.

Difference in the Susceptibility Degree	Difference between the T-LSM and RLSM		Difference between the D-LSM and D-RLSM	
	No. of Cells	%	No. of Cells	%
0	7,171,591	98.7635	7,165,205	98.6756
+1	60,305	0.8305	64,922	0.8941
+2	19,354	0.2666	20,686	0.2849
+3	10,125	0.1394	10,562	0.1455

Table 10. Overview of the differences among the T-LSM, T-RLSM, and D-RLSM.

Difference in the Susceptibility Degree	Difference between the T-LSM and RLSM		Difference between the D-LSM and D-RLSM	
	No. of Cells	%	No. of Cells	%
−2	972	0.01339	972	0.01339
−1	996,480	13.7230	996,480	13.7230
0	5,628,187	77.5086	5717,971	78.7450
+1	606,255	8.34900	545,950	7.5186
+2	19,356	0.2666	2	0.00003
+3	10,125	0.1394		

The results show that the inclusion of surface deformation information does not cause the area of each susceptibility degree in the resulting LSM to vary significantly; nevertheless, after integrating both the soil moisture and MT-InSAR datasets, nearly a quarter of the study area experienced a susceptibility degree increase or decrease compared to the T-LSM and T-RLSM, indicating dynamic conditions.

To assess the correlation between actual landslides and the RLSMs, we linked the historical landslide dataset used to train the model and the new landslide dataset used for validation to calculate their landslide density index values relative to the RLSMs. To ensure the reliability of the results, only the corresponding datasets were used in this procedure to test the landslide fitting degree of the T-RLSM and rainy-season D-RLSM. Figure 16a shows the landslide fit test results derived using the historical landslide data recorded during the rainy season. Whether the LSM or RLSM was being assessed, the relative landslide density index discrepancies derived between the maps under the same susceptibility class were very small. The maximum disparity reached only 3.0851%. In contrast, the index obtained for the very high susceptibility class was much greater than the corresponding indices in the other three categories, and the maximum difference reached 84.5033%. Figure 16b shows imagery of the indices derived based on the validation landslide dataset. In this context, the indices shown in the four low-susceptibility graphs are small and similar. The index inconsistencies between the LSMs and the RLSMs increased as the susceptibility degree increased, starting from the medium susceptibility degree and reaching a maximum of 28.6899%. Notably, the inconspicuous index differences between the RLSMs and the LSMs shown in Figure 16a are small. In addition, a phenomenon described above is again magnified here; in short, the very-high-susceptibility classes in the RLSMs predict landslides with a higher accuracy than those in the LSMs. Clearly, the relative landslide density index of each LSM/RLSM exhibits the same trend under the two landslide datasets, and both show the characteristic of increasing with the susceptibility degree. Nonetheless, the differences between these indices were significant between the different landslide datasets, especially when assessing the validation set. This outcome suggests that the very-high-susceptibility areas in the RLSMs tended to experience landslides more often than the corresponding areas in the LSMs, while other susceptibility areas exhibited the opposite trend; that is, the landslide predictions provided by the RLSMs were more reliable than those derived from the LSMs.

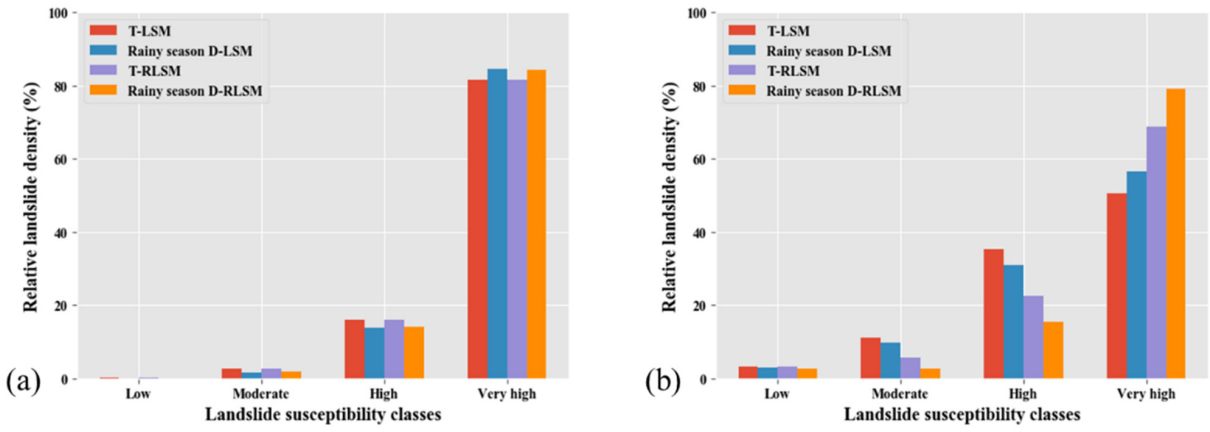

Figure 16. Relative landslide density index values of the obtained LSMs and RLSMs: (**a**) the relative historical landslide density index in the rainy season and (**b**) the relative new landslide density index.

5.4. Results of Specific Case Studies

In summary, most of the pixels that exhibited increased susceptibility degrees were distributed in the western and southeastern regions of the study area, whereas most of the pixels with decreased susceptibility degrees were distributed in the northern and central regions. Therefore, we selected three specific slopes in Dongfeng town, Haila town, and Dajie township as examples for a brief discussion.

5.4.1. Dongfeng Town

Dongfeng town is located in southeastern Weining and is characterized by terrain that is high in the north and low in the south. The slope analyzed herein is located in Yuanmudi and Huangni Villages, along the southeastern edge of Dongfeng. The coordinates are 104°34′31″–104°34′41″ E and 26°48′3″–26°48′11″ N. In Figure 17, the purple vector boundary represents the boundary of the slope; this boundary was obtained by identifying the intersection of the ridge line and the valley line. The T-LSM results (Figure 17a) show that the slope is dominated by moderate susceptibility. According to the statistical results (Figure 18), only approximately 3.57% of the pixels were predicted to have very high susceptibility; that is, the possibility of landslides occurring on this slope is small. In the D-LSM (Figure 17b), the number of high-susceptibility cells in this region increased significantly, accounting for approximately 71.43% of the area. However, the scale of very-high-susceptibility cells was still as low as 12.5%. Due to the complex geological and geomorphological conditions in the surrounding area and the frequent occurrence of historical landslide disasters, the prediction of a great number of very-high-susceptibility units around this slope is consistent with the actual records, while the quantities of very-high-susceptibility pixels in the field of view and the slope body are close to those exhibited by the T-LSM. Nevertheless, the MT-InSAR dataset (Figure 17c) expressed that this slope is active from top to toe, and the maximum V_{slope} value was higher than 24 mm/year, suggesting ultrahigh-speed deformation. The refined D-RLSM (Figure 17d) rectified the very-high-susceptibility regions that were not forecasted in the LSMs, allowing their proportion to increase by 42.8572% and 33.9286% compared to the T-LSM and D-LSM, respectively.

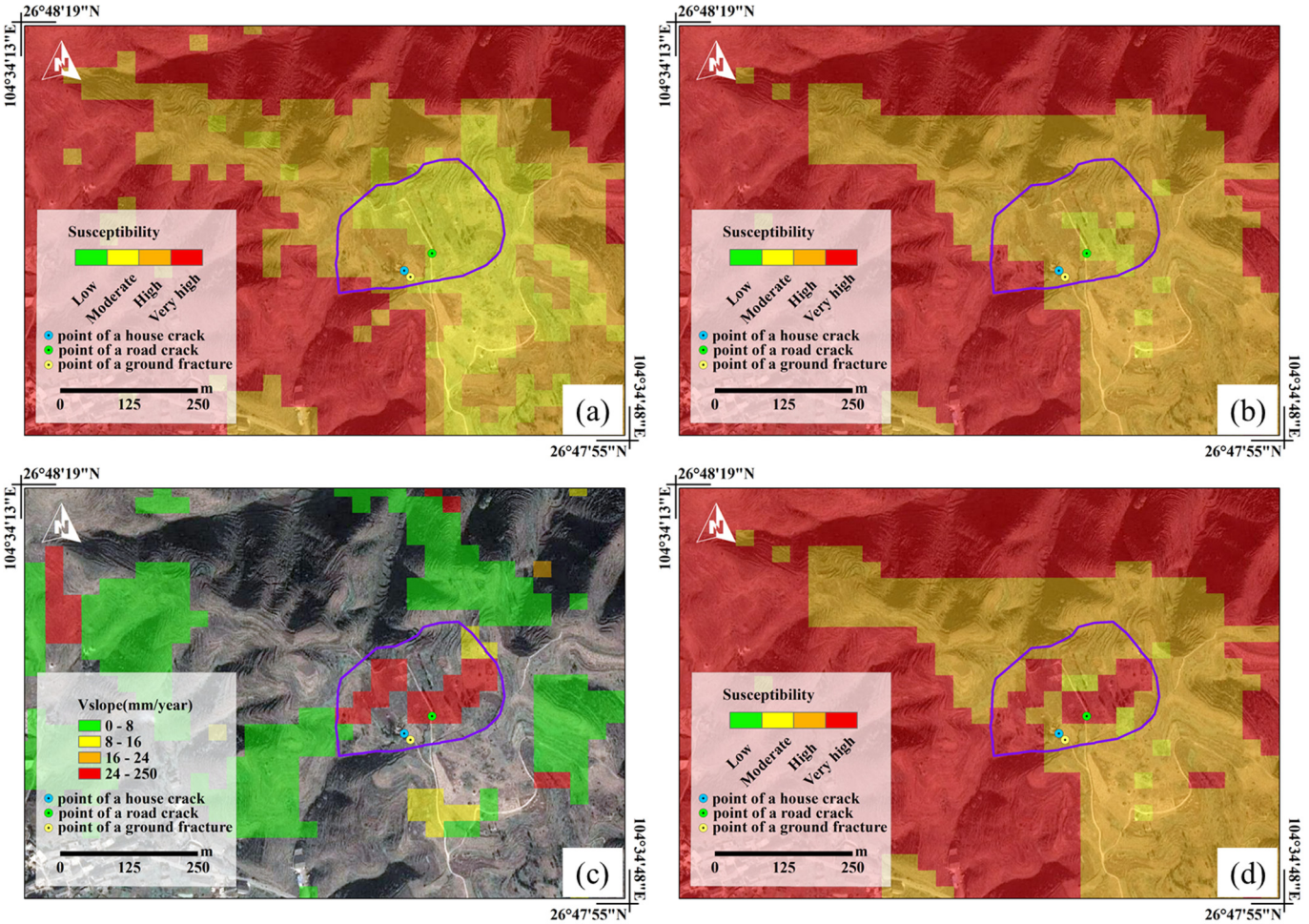

Figure 17. Results obtained for the landslide susceptibility of Dongfeng town in each stage: (**a**) the T-LSM; (**b**) the rainy-season D-LSM; (**c**) the V_{slope} distribution; and (**d**) the D-RLSM.

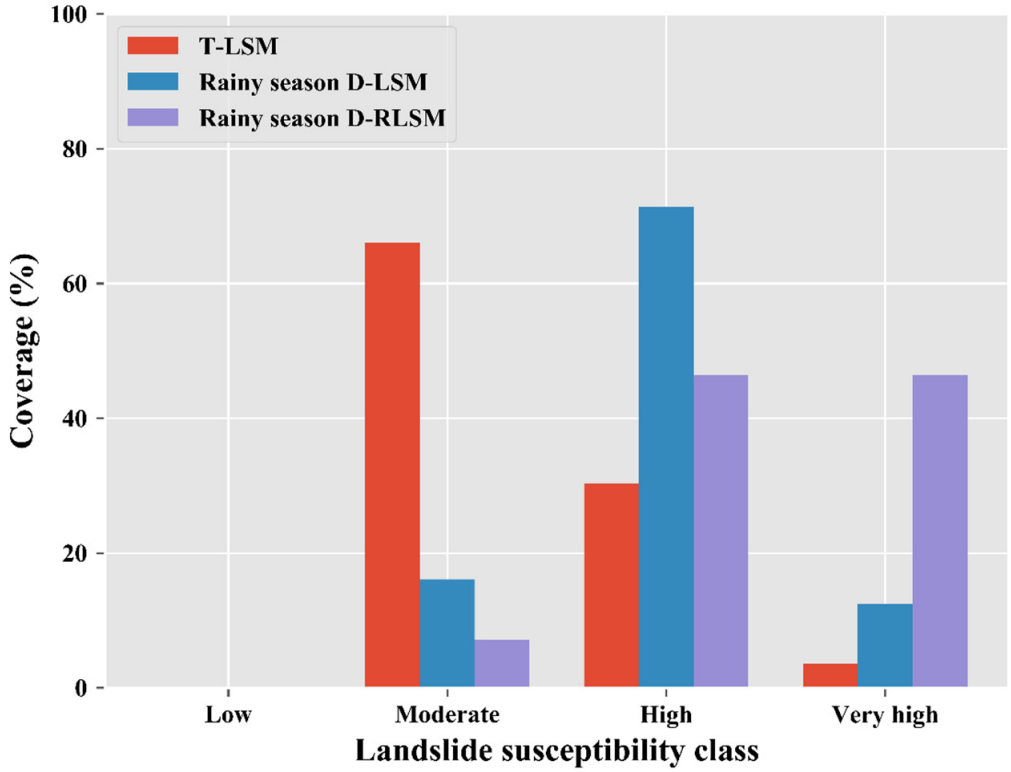

Figure 18. Landslide susceptibility coverage rates in Dongfeng town.

To validate the above results, a field investigation was performed in the monitoring range (Figure 19a). The landform of interest is an eroded low- and medium-sloping mountain; the slope faces northwest; the maximum elevation disparity is approximately 100 m; the top of the mountain slopes gently, representing a platform with a slope of 5°–10°; and the slope in the valley typically ranges from 20°–30° with local slopes greater than 40°. The Quaternary residual slope contains 0–2 m thick gravels and silts, and the lower part of the slope contains Permian Yangxin Longtan Formation (P3l) mudstones and siltstones intercalated with coal. At the same time, the middle and upper regions of the slope contain the argillaceous siltstone of the Feixianguan Formation of the Lower Triassic System (T1f), which has a rock formation of 170°∠8°, two groups of joints developed at 200°∠70° and 140°∠75°, and bedrock that is strongly weathered and broken. Tensile cracks are densely developed on the ground in the middle and upper regions of the slope (Figure 19b); these cracks are 10–30 cm wide, 2 m deep, and 10–20 m long, with 3–12 cm subsidence. Multiple fractures have appeared in the mechanical tillage road (Figure 19c), and some houses in Huangni Village have been damaged by these pulling cracks (Figure 19d). The Dongfeng Xijing Coal Mine Area of the Water Mining Group is located on the southern periphery of this monitoring area. Thus, it is speculated that the slope cracking and subsidence observed in this region are mainly caused by the goaf and rainfall.

Based on the on-site investigation and interviews, the stability of the deformation area of this slope is poor, and there is a high possibility of landslide danger. Although no landslides have yet occurred on this slope, the actual deformation situation cannot be ignored. The susceptibility class of this area should be divided into the very high class, as suggested by the D-RLSM. Thus, we suggest the continuous monitoring of this slope. Namely, in the case that the RF model cannot properly predict the susceptibility class of this slope, the D-RLSM refined by the correction matrix could be used to reduce the omission rates when forecasting landslides using LSMs.

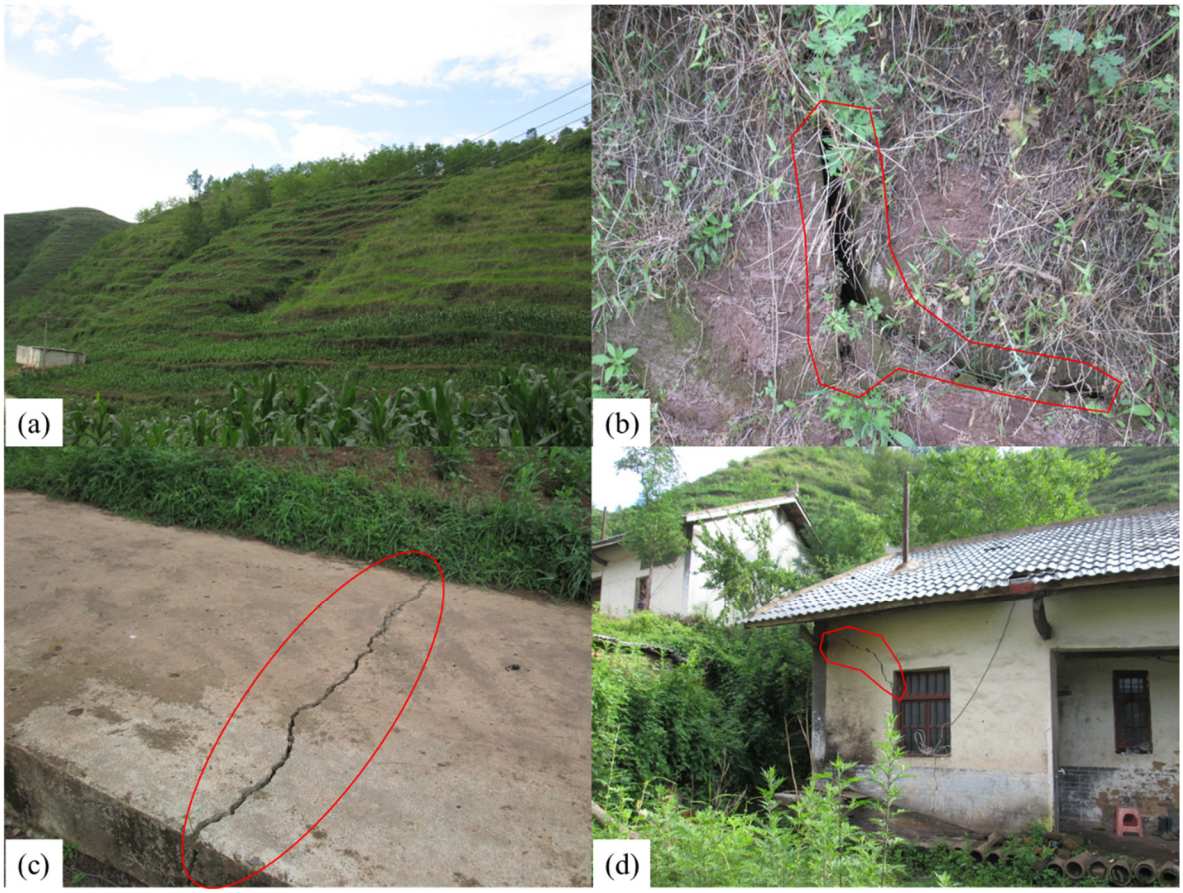

Figure 19. Field investigation map of Dongfeng town: (**a**) the slope of interest; (**b**) a ground fracture (the yellow point in Figure 17); (**c**) a road crack (the green point in Figure 17); and (**d**) a house crack (the blue point in Figure 17).

5.4.2. Haila Town

Haila town is located in western Weining County. The terrain in this region is low on the periphery and high in the middle. The slope of concern in this work is located at the western edge of Haila town, across the Niulan River from Huohong township, in Yunnan Province. In Figure 17, the purple vector represents the boundary of the slope. In detail, a complex small landslide was reported on the upper part of the S1 slope in 2019, at the coordinates of 103°43′49″–103°44′22″ E and 26°46′18″–26°46′47″ N. The slope faces northwest, the maximum slope degree is approximately 32°, and the maximum elevation difference is approximately 310 m. According to the D-RLSM results (Figure 20d), most of the pixels in the upper part of the slope are characterized by the very-high-susceptibility class, while the middle and lower parts of the slope mainly correspond to high susceptibility. Based on the premise that the T-LSM scarcely changes over long timeframes, the T-LSM (Figure 20a) exhibited many cells with very high susceptibility in the current field of view. However, most of the evaluation units showed low and medium susceptibility levels in the upper part of S1, suggesting inconsistencies with the field survey results. The areas predicted as being of high and very high susceptibility did not have reported events or signs of landslides, while areas corresponding to low and medium susceptibility had experienced landslides or showed signs of landslides in the past; these findings represent the manifestations of false alarm and omissions, respectively. Thus, in the D-LSM (Figure 20b), in which SMAP-R dynamic data were incorporated, the false alarm rate was vastly diminished as the quantities of high- and very-high-susceptibility cells decreased. The statistics of the coverage ratio of each class (Figure 21) illustrated that within the range of slope S1, the very-high-susceptibility regions of the D-RLSM accounted for

approximately 25.6566% of the entire slope, 9.0909% more than those areas indicated by the LSM and D-LSM, while the areal proportions of the other three susceptibility degrees were slightly lower than those reflected in the LSM and D-LSM. Next, the MT-InSAR dataset was analyzed, highlighting a different scenario (Figure 20c) in which the PS/DS displacement information confirmed that the upper part of the S1 slope was active as well as the S2 slope; in addition, the maximum V_{slope} value was higher than 24 mm/year. Although the S2 slope has not yet been exposed to landslide dangers, its rapid deformation and potential for landslides must be considered. Furthermore, the displacement information shows that the susceptibility of the upper part of the slope was significantly controlled by the surface deformation information, which could not be suitably predicted by the RF method; thus, the benefit obtained by refining the LSM with the correction matrix is obvious. Considering the SMAP-R dataset and the areas highlighted in the MT-InSAR map, the D-RLSM represents the optimal prediction of slow-moving landslides among the LSMs derived herein.

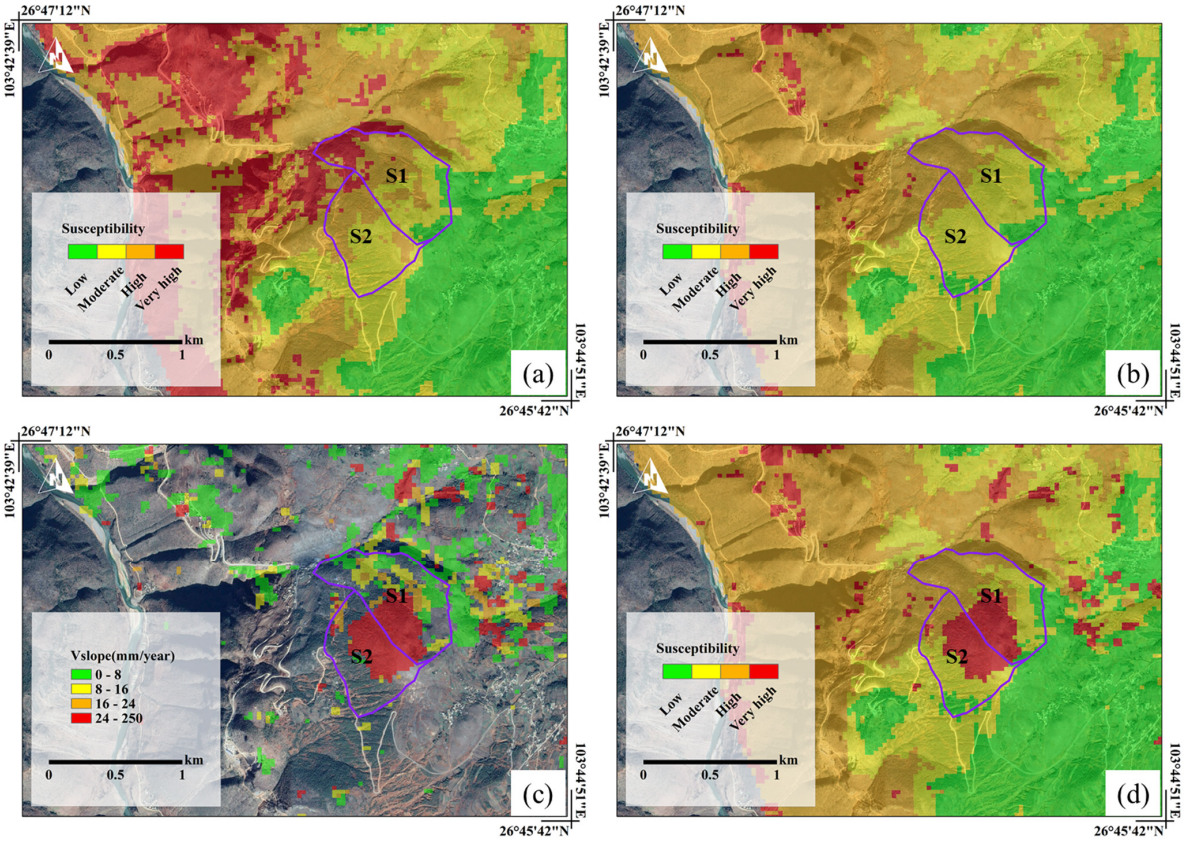

Figure 20. Results obtained for Haila township in each stage: (**a**) the T-LSM; (**b**) the rainy-season D-LSM; (**c**) the V_{slope} distribution; and (**d**) the D-RLSM.

5.4.3. Dajie Township

Dajie township lies in the northeast region of Weining County. The terrain is high in the northwest and low in the southeast. The hillside we are interested in with regards to this work is located in the middle of Dajie township. In Figure 22, the purple polygon represents the vector boundaries of the slope of interest. This slope is located between 104°13′24″ and 104°14′6″ E and between 27°4′40″ and 27°5′8″ N. The slope faces south, has a maximum slope angle of approximately 36°, and has a maximum elevation disparity of approximately 200 m. No landslides have been reported on this slope to date. Conversely, the T-LSM (Figure 22a) exhibited very high susceptibility degrees for many cells on the target slope and on other slopes or in other regions within the current window, thus increasing the predicted false alarm rate for landslides. In addition, the derived PS/DS displacement

information suggests that this slope is basically steady. Compared to the T-LSM, the scale of the very-high-susceptibility units in the D-LSM and D-RLSM was reduced by approximately 60% (Figure 23). In this case, the D-RLSM (Figure 22d) created from the D-LSM (Figure 22b) based on the dynamic information contained in the SMAP-R dataset and V_{slope} map (Figure 22c) is indispensable and immediately enhances the landslide prediction accuracy by reducing the false alarm rate and omission rate.

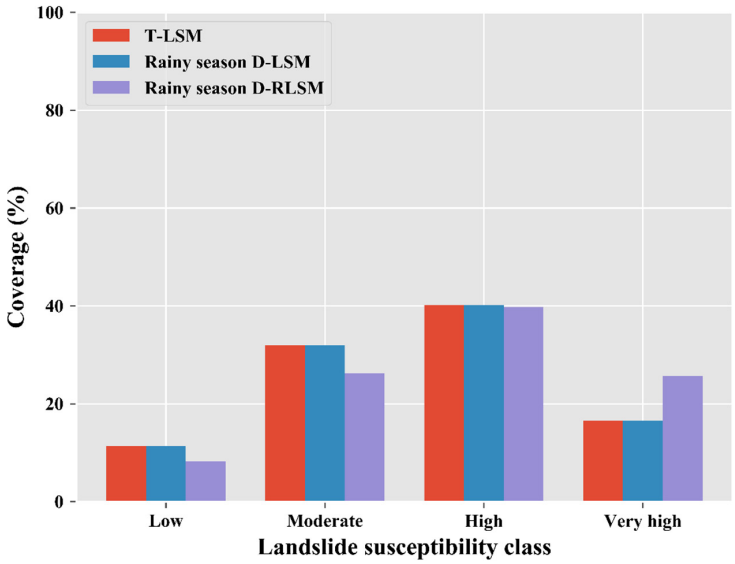

Figure 21. Landslide susceptibility coverage rates in Haila town.

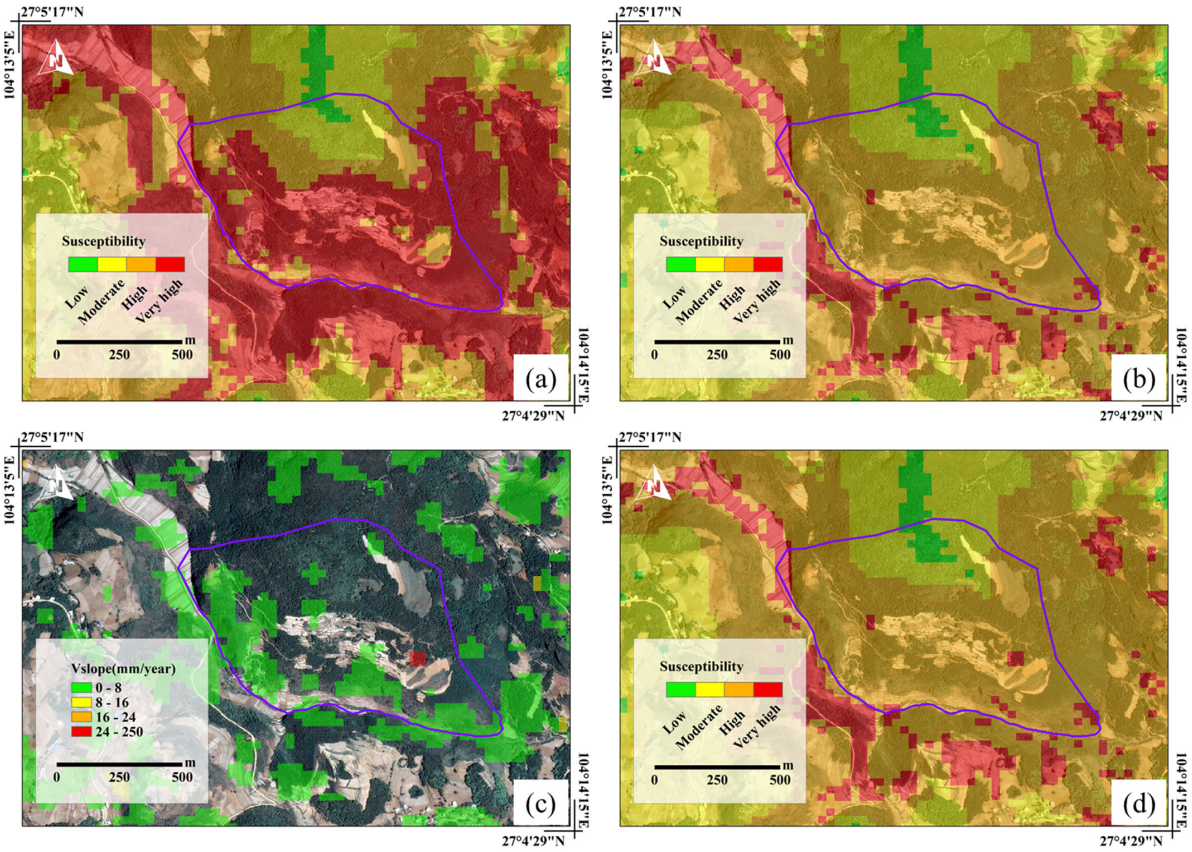

Figure 22. Results obtained for Dajie township in each stage: (**a**) the T-LSM; (**b**) the rainy-season D-LSM; (**c**) the V_{slope} distribution; and (**d**) the D-RLSM.

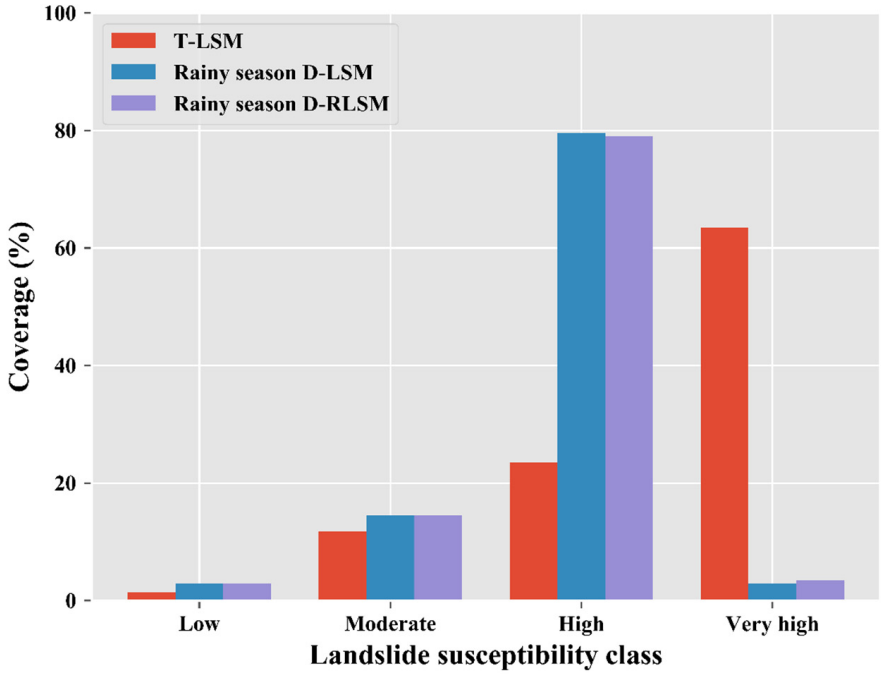

Figure 23. Landslide susceptibility coverage rates in Dajie township.

6. Discussion

6.1. D-LSM

Soil moisture conditions play a crucial role in the occurrence of landslides. By combining soil moisture data with LSMs, researchers can dynamically update and correct landslide susceptibility degrees in areas affected by soil moisture, thereby reducing the LSM's false alarm rate and improving the LSM's reliability. The high- and very-high-susceptibility areas indicated by the T-LSM predicted by the RF model surrounded the study area, while the very-high-susceptibility areas indicated by the D-LSM were mainly concentrated around the four diagonal corners. Comparing the T-LSM generated using traditional static factors with the D-LSMs obtained while considering soil moisture conditions, the addition of soil moisture conditions resulted in susceptibility level changes in nearly one-quarter of the cells. Variations in soil moisture are accompanied by fluctuations in landslide susceptibility. The rainy-season D-LSM exhibited susceptibility changes in 20% of the units compared to the dry-season D-LSM. Through the statistics obtained by comparing the T-LSM with the D-LSM linked with the landslide dataset, we found that the fitting degree of these two LSMs in the new landslide dataset was lower than that of the historical landslide dataset. Nevertheless, the latter still had a higher fitting degree than the former in each susceptibility class due to the former containing nearly one-fifth fewer units in the very-high-susceptibility class than the latter. Regarding the new landslide dataset, the relative landslide density index difference of the T-LSM was larger than the value calculated using the historical landslide dataset. Specifically, the validity and reliability of the D-LSM were better than those of the T-LSM when predicting landslides in the future.

However, the D-LSM has certain limitations. First, landslide samples are the basis for training the model. Therefore, the input landslide dataset requires highly accurate spatiotemporal information and detailed property descriptions to maintain spatial and temporal consistency with soil moisture products, as well as to ensure the applicability of the soil moisture products to the research object. Second, the SMAP-R, derived from the satellite remote sensing retrieval method, provides relatively temporally and spatially complete soil moisture information on a national or even global scale. However, the spatial resolution of these data becomes slightly rough when the scale of the observation object shrinks to a city or county. With the intention of improving the spatial resolution of the SMAP-R data, appropriate interpolation and resampling methods must be considered. If

necessary, optimization by referring to field measurements or establishing a hydrological model [68] is recommended. In addition, the SMAP-R data contain root zone soil moisture information estimated by combining the surface microwave radiation (or brightness temperature) and radar backscattering measured by the sensor with other auxiliary data (e.g., meteorological data and surface properties and parameters). During this procedure, estimation inaccuracies and errors occur due to the inevitable errors present in each stage, thus introducing uncertainty in subsequent applications. Hence, it is necessary to consider this potential defect as well as its direct and indirect effects. Under certain conditions, actual observations may be introduced to ameliorate this problem.

6.2. RLSM

MT-InSAR can be used to identify only surface motion and temporarily ignore landslides in the absence of displacement. On the other hand, LSMs use only some explicit deformation features and have limitations when estimating the recent activities of individual landslides. Therefore, by combining LSMs with MT-InSAR, the landslide susceptibility degrees of areas affected by surface deformation can be refined and corrected in a targeted manner to improve the LSM's accuracy. Similar to the LSMs predicted by the RF model, the distribution of each susceptibility class in the RLSMs is approximately the same. However, the MT-InSAR technique produces contrasting monitoring results in the time series images. For example, in some areas with low, medium, or even high susceptibility, large V_{slope} values indicate that the slopes are active. In this case, we may increase the susceptibility degree of the areas affected by ground deformation, as highlighted in the average deformation rate map characterizing the steepest aspect projected from the MT-InSAR data. By comparing the LSMs and RLSMs, it can be found that the RLSMs correct the susceptibility in approximately 1.3% of the evaluation units, most of which are distributed in the central and western parts of the study area. The relative landslide density index values of the RLSMs and LSMs show that using disparate landslide datasets provides visual feedback, suggesting that the former is exponentially lower than the latter. Looking beyond the appearance to see the essence, "very high susceptibility" suggests the greatest likelihood of landslide occurrence. The higher the degree of fit, the more accurate the result is. Otherwise, the lower the susceptibility, the less likely a landslide will occur. The lower the fitting degree, the more reasonable the prognostication is. The testing of the utilized models with the historical landslide dataset is, in turn, a verification of the fit of historical landslides, while the new landslide dataset is used to verify the fit of anticipated landslides. To put it simply, the prediction accuracies of the LSMs and RLSMs are very high and similar when compared to historical landslides. In contrast, the accuracies of the RLSMs are greatly increased compared to those of the LSMs when assessing new landslides.

Having said that, this work also has some restrictions. First, it is difficult to apply the MT-InSAR technique to measure surface deformation associated with large movement rates or intense seasonal variations (usually faster than 10–20 cm/year) [32], mainly due to the wavelength of the radar and the revisit period of the platform. Therefore, the pixel offset tracking method can be applied as a complement to the MT-InSAR dataset; this method is based on the cross-correlation of SAR image amplitude values and has been shown to be an effective tool for measuring large displacement velocities [69] and reducing temporal decoherence using relatively high-temporal-resolution data. Second, the geometry-related limitations of SAR imagery largely affect the application of InSAR technology in mountainous areas due to topographic factors such as oblique range imaging, overlapping, and shadowing. When the LOS direction is unfavorable to the assessment of surface deformation, it may reduce the quantity of available measurement points or even result in no available points. To improve this situation, data could be obtained from different orbits (ascending or descending) and sensors and included in analyses. Next, systematic errors may occur in densely vegetated mountainous areas due to the inherent limitations of SAR technology. One of the solutions to this problem is to utilize relatively long radar wavelength data to minimize the correlation effects caused by vegetation cover

and ameliorate radar signal penetration. Alternatively, PSs and DSs can be combined to make full use of InSAR stack data, thus reducing noise and increasing the scatterer density with the aim of improving the displacement monitoring of hills covered by pastures, shrubs, and bare soils.

7. Conclusions

LSMs represent basic tools used in landslide hazard risk assessments and management measures, urban planning, and land resource management. To advance the reliability and timeliness of LSMs while reducing their false alarm rate and omission rate, in this paper we propose a new method for dynamically refining LSMs by integrating SMAP-R products and the MT-InSAR dataset.

In this study, we considered 12 static parameters, such as the slope, aspect, and curvature, and SMAP-R as a dynamic factor when constructing a landslide susceptibility evaluation system. With these parameters, the RF algorithm in the sklearn package of Python was used to generate three LSMs representing Weining County, Guizhou Province, at an evaluation unit resolution of 30 × 30 m. The ROC and relative landslide density index analyses showed that the LSM in which the SMAP-R factor was introduced had the best AUC value (0.9132) and a relatively high landslide fit (56.5470%), thus indicating that SMAP-R improved the landslide prediction accuracy obtained using LSMs in the study area and increased the reliability of these LSMs. The variations in the SMAP-R data were used to construct different LSMs, and the false alarm rate of the resulting T-LSM was reduced to a certain extent. Essentially, SMAP-R data has the ability to dynamically update LSMs, making near-real-time or even real-time landslide predictions possible.

An MT-InSAR analysis was also implemented in Weining County using the acquired 2018 Sentinel-1A dataset to obtain the PS/DS deformation along the LOS direction. Furthermore, the average deformation rate was calculated along the steepest slope to prevent the effects of geometric distortion. Next, the data were resampled to the same resolution as the LSMs. A correction matrix was established depending on the susceptibility and velocity to determine the final susceptibility class corresponding to each evaluation unit under the impact of the MT-InSAR measurements. This process induced susceptibility changes in approximately 1.2365% and 1.3244% of the pixels in the T-LSM and D-LSM, respectively. The comparison of the D-RLSM with the T-LSM showed that the original susceptibility degree of the region within a total area of approximately 1416.5 km^2 either increased or decreased. The outcomes of the relative landslide density index conveyed that the landslide prediction accuracy of the D-RLSM (79.2323%) was greatly increased compared to that of the LSM; in addition, the false alarm rate of the D-RLSM was greatly reduced.

That is, the D-RLSM generated using the method proposed herein allowed for more targeted landslide predictions with higher reliabilities and timeliness, as well as lower false alarm and omission rates.

This process can be easily applied in different regions where SMAP-R and MT-InSAR datasets are available. The method proposed herein will assist planning and decision-making departments/units in producing reliable LSMs.

Author Contributions: Conceptualization, Z.C. and C.X.; data curation, Q.Y.; methodology, Q.Y. and C.X.; software, H.F. and B.T.; validation, C.S., D.Z. and X.Y.; investigation, G.C. and T.X.; writing—original draft preparation, Q.Y.; writing—review and editing, Z.C. and C.X.; supervision, Z.C., C.X. and C.S.; project administration, Y.G. and Y.Z.; funding acquisition, C.X. and C.S. All authors have read and agreed to the published version of the manuscript.

Funding: This research was funded by the National Key R&D Program of China (grant number 2022YFC3005601), the Outstanding Youth Science and Technology Program of Guizhou Province of China (grant number [2021]5615), and the Multi-source remote sensing regional landslide hazard risk mapping and key landslide Fine Survey of the STS Program of Fujian Province of China (grant number 2020T3011).

Data Availability Statement: Sentinel-1 data were provided by ESA, Europe. The SMAP L4 data were provided by the National Aeronautics and Space Administration (NASA) National Snow and Ice Data Center Distributed Active Archive Center. The Geological map of Weining is unavailable due to local privacy. The one-arc-second SRTM DEM was freely downloaded from the website http://e4ftl01.cr.usgs.gov/MODV6_Dal_D/SRTM/SRTMGL1.003/2000.02.11/ (accessed on 26 October 2021). The GlobeLand30 land cover data was freely downloaded from the website http://www.globallandcover.com (accessed on 31 October 2021).

Acknowledgments: The authors would like to thank the Copernicus program for the free access to Sentinel-1 images processed in this analysis.

Conflicts of Interest: The authors declare no conflict of interest.

References

1. National Bureau of Statistics of China. *China Statistical Yearbook*; National Bureau of Statistics of China: Beijing, China, 2021.
2. Kjekstad, O.; Highland, L. Economic and Social Impacts of Landslides. In *Landslides—Disaster Risk Reduction*; Springer: Berlin/Heidelberg, Germany, 2009; pp. 573–587.
3. Xu, H.; Ma, C.; Lian, J.; Xu, K.; Chaima, E.J. Urban flooding risk assessment based on an integrated k-means cluster algorithm and improved entropy weight method in the region of Haikou, China. *J. Hydrol.* **2018**, *563*, 975–986. [CrossRef]
4. Zou, Q.; Cui, P.; He, J.; Lei, Y.; Li, S.J.G. Regional risk assessment of debris flows in China—An HRU-based approach. *Geomorphology* **2019**, *340*, 84–102. [CrossRef]
5. Sun, R.; Gong, Z.; Gao, G.; Shah, A.A. Comparative analysis of Multi-Criteria Decision-Making methods for flood disaster risk in the Yangtze River Delta. *Int. J. Disaster Risk Reduct.* **2020**, *51*, 101768. [CrossRef]
6. Brabb, E.E. Innovative approaches to landslide hazard and risk mapping. In Proceedings of the 4th International Symposium on Landslides, Toronto, ON, Canada, 23–31 August 1985.
7. Rossi, M.; Guzzetti, F.; Reichenbach, P.; Mondini, A.C.; Peruccacci, S.J.G. Optimal landslide susceptibility zonation based on multiple forecasts. *Geomorphology* **2010**, *114*, 129–142. [CrossRef]
8. Althuwaynee, O.F.; Pradhan, B.; Park, H.-J.; Lee, J.H. A novel ensemble bivariate statistical evidential belief function with knowledge-based analytical hierarchy process and multivariate statistical logistic regression for landslide susceptibility mapping. *Catena* **2014**, *114*, 21–36. [CrossRef]
9. Tian, M.; Xiaolu, X.; Hanhu, L.J. Landslide risk assessment in high altitude areas based on slope unit optimization: Taking the Baige landslide in Jinsha River as an example. *J. Henan Polytech. Univ.* **2021**, *40*, 65–72.
10. Lee, S.; Min, K. Statistical analysis of landslide susceptibility at Yongin, Korea. *Environ. Geol.* **2001**, *40*, 1095–1113. [CrossRef]
11. Yalcin, A.; Reis, S.; Aydinoglu, A.; Yomralioglu, T.J.C. A GIS-based comparative study of frequency ratio, analytical hierarchy process, bivariate statistics and logistics regression methods for landslide susceptibility mapping in Trabzon, NE Turkey. *Catena* **2011**, *85*, 274–287. [CrossRef]
12. Yu, X.; Gao, H.J. A landslide susceptibility map based on spatial scale segmentation: A case study at Zigui-Badong in the Three Gorges Reservoir Area, China. *PLoS ONE* **2020**, *15*, e0229818. [CrossRef]
13. Piciullo, L.; Calvello, M.; Cepeda, J.M. Territorial early warning systems for rainfall-induced landslides. *Earth Sci. Rev.* **2018**, *179*, 228–247. [CrossRef]
14. Caine, N.J. The rainfall intensity-duration control of shallow landslides and debris flows. *Geogr. Ann.* **1980**, *62*, 23–27.
15. Teja, T.S.; Dikshit, A.; Satyam, N.J. Determination of rainfall thresholds for landslide prediction using an algorithm-based approach: Case study in the Darjeeling Himalayas, India. *Geosciences* **2019**, *9*, 302. [CrossRef]
16. Chleborad, A.F. *Preliminary Evaluation of a Precipitation Threshold for Anticipating the Occurrence of Landslides in the Seattle, Washington, Area*; USGS: Washington, DC, USA, 2003; Volume 3, p. 39.
17. Calvello, M.; d'Orsi, R.N.; Piciullo, L.; Paes, N.; Magalhaes, M.; Lacerda, W.A. The Rio de Janeiro early warning system for rainfall-induced landslides: Analysis of performance for the years 2010–2013. *Int. J. Disaster Risk Reduct.* **2015**, *12*, 3–15. [CrossRef]
18. Zhuo, L.; Dai, Q.; Han, D.; Chen, N.; Zhao, B.; Berti, M.J.; Sensing, R. Evaluation of remotely sensed soil moisture for landslide hazard assessment. *IEEE J. Sel. Top. Appl. Earth Obs. Remote Sens.* **2019**, *12*, 162–173. [CrossRef]
19. Zhuo, L.; Han, D.J. Misrepresentation and amendment of soil moisture in conceptual hydrological modelling. *J. Hydrol.* **2016**, *535*, 637–651. [CrossRef]
20. Pelletier, J.D.; Malamud, B.D.; Blodgett, T.; Turcotte, D. Scale-invariance of soil moisture variability and its implications for the frequency-size distribution of landslides. *Eng. Geol.* **1997**, *48*, 255–268. [CrossRef]
21. Ray, R.L.; Jacobs, J.M.; Cosh, M. Landslide susceptibility mapping using downscaled AMSR-E soil moisture: A case study from Cleveland Corral, California, US. *Remote Sens. Environ.* **2010**, *114*, 2624–2636. [CrossRef]
22. Ray, R.L.; Jacobs, J.M.; Ballestero, T. Regional landslide susceptibility: Spatiotemporal variations under dynamic soil moisture conditions. *Nat. Hazards* **2011**, *59*, 1317–1337. [CrossRef]
23. Abraham, M.T.; Satyam, N.; Rosi, A.; Pradhan, B.; Segoni, S.J.C. Usage of antecedent soil moisture for improving the performance of rainfall thresholds for landslide early warning. *Catena* **2021**, *200*, 105147. [CrossRef]

24. Pratola, C.; Barrett, B.; Gruber, A.; Kiely, G.; Dwyer, E. Evaluation of a global soil moisture product from finer spatial resolution SAR data and ground measurements at Irish sites. *Remote Sens.* **2014**, *6*, 8190–8219. [CrossRef]
25. Albergel, C.; Dorigo, W.; Reichle, R.; Balsamo, G.; De Rosnay, P.; Muñoz-Sabater, J.; Isaksen, L.; De Jeu, R.; Wagner, W.J. Skill and global trend analysis of soil moisture from reanalyses and microwave remote sensing. *J. Hydrometeorol.* **2013**, *14*, 1259–1277. [CrossRef]
26. An, R.; Zhang, L.; Wang, Z.; Quaye-Ballard, J.A.; You, J.; Shen, X.; Gao, W.; Huang, L.; Zhao, Y.; Ke, Z.J.; et al. Validation of the ESA CCI soil moisture product in China. *Int. J. Appl. Earth Obs. Geoinf.* **2016**, *48*, 28–36. [CrossRef]
27. Zhao, B.; Dai, Q.; Zhuo, L.; Zhu, S.; Shen, Q.; Han, D.J. Assessing the potential of different satellite soil moisture products in landslide hazard assessment. *Remote Sens. Environ.* **2021**, *264*, 112583. [CrossRef]
28. Wang, C.; Cai, J.; Li, Z.; Mao, X.; Feng, G.; Wang, Q.J. Kinematic parameter inversion of the slumgullion landslide using the time series offset tracking method with UAVSAR data. *J. Geophys. Res. Solid Earth* **2018**, *123*, 8110–8124. [CrossRef]
29. Dong, J.; Zhang, L.; Li, M.; Yu, Y.; Liao, M.; Gong, J.; Luo, H.J.L. Measuring precursory movements of the recent Xinmo landslide in Mao County, China with Sentinel-1 and ALOS-2 PALSAR-2 datasets. *Landslides* **2018**, *15*, 135–144. [CrossRef]
30. Lu, P.; Catani, F.; Tofani, V.; Casagli, N.J.L. Quantitative hazard and risk assessment for slow-moving landslides from Persistent Scatterer Interferometry. *Landslides* **2014**, *11*, 685–696. [CrossRef]
31. Colesanti, C.; Ferretti, A.; Prati, C.; Rocca, F.J. Monitoring landslides and tectonic motions with the Permanent Scatterers Technique. *Eng. Geol.* **2003**, *68*, 3–14. [CrossRef]
32. Wasowski, J.; Bovenga, F.J. Investigating landslides and unstable slopes with satellite Multi Temporal Interferometry: Current issues and future perspectives. *Eng. Geol.* **2014**, *174*, 103–138. [CrossRef]
33. Bekaert, D.P.; Handwerger, A.L.; Agram, P.; Kirschbaum, D. InSAR-based detection method for mapping and monitoring slow-moving landslides in remote regions with steep and mountainous terrain: An application to Nepal. *Remote Sens. Environ.* **2020**, *249*, 111983. [CrossRef]
34. Nico, G.; Oliveira, S.; Catalão, J.; Zêzere, J.; Garcia, R. Landslide susceptibility mapping based on Persistent Scatterers inventories. In Proceedings of the ESA Living Planet Symposium, Bergen, Norway, 28 June–2 July 2010; p. 327.
35. Oliveira, S.; Zêzere, J.; Catalão, J.; Nico, G.J.L. The contribution of PSInSAR interferometry to landslide hazard in weak rock-dominated areas. *Landslides* **2015**, *12*, 703–719. [CrossRef]
36. Piacentini, D.; Devoto, S.; Mantovani, M.; Pasuto, A.; Prampolini, M.; Soldati, M.J.N.H. Landslide susceptibility modeling assisted by Persistent Scatterers Interferometry (PSI): An example from the northwestern coast of Malta. *Nat. Hazards* **2015**, *78*, 681–697. [CrossRef]
37. Shao, L.; Li, J. Evaluating the Geo-Hazard in Weining county, Guizhou. *Geol. Hazards Environ. Prot.* **2012**, *23*, 27–31+54.
38. Bureau of Geology and Mineral Exploration and Development Guizhou Province. *Regional Geology of Guizhou Province*; Geological Publishing House: Beijing, China, 1987.
39. Yang, S.-Y.; Zhang, J.-J. *Environmental Geology of Guizhou*; Guizhou Science and Technology Publishing House: Guiyang, China, 2008.
40. Liu, H.; Long, S. Geo-Hazard investigation and evaluation for Weining county, Guizhou. *Geol. Hazards Environ. Prot.* **2012**, *23*, 21–25.
41. Sun, D.; Wen, H.; Wang, D.; Xu, J.J. A random forest model of landslide susceptibility mapping based on hyperparameter optimization using Bayes algorithm. *Geomorphology* **2020**, *362*, 107201. [CrossRef]
42. Guzzetti, F.; Mondini, A.C.; Cardinali, M.; Fiorucci, F.; Santangelo, M.; Chang, K. Landslide inventory maps: New tools for an old problem. *Earth-Sci. Rev.* **2012**, *112*, 42–66. [CrossRef]
43. Reichenbach, P.; Rossi, M.; Malamud, B.D.; Mihir, M.; Guzzetti, F.J. A review of statistically-based landslide susceptibility models. *Earth Sci. Rev.* **2018**, *180*, 60–91. [CrossRef]
44. Dai, F.; Lee, C.; Li, J.; Xu, Z. Assessment of landslide susceptibility on the natural terrain of Lantau Island, Hong Kong. *Environ. Geol.* **2001**, *40*, 381–391.
45. Lee, S.J. Application of logistic regression model and its validation for landslide susceptibility mapping using GIS and remote sensing data. *Int. J. Remote Sens.* **2005**, *26*, 1477–1491. [CrossRef]
46. Zhou, X.; Wen, H.; Zhang, Y.; Xu, J.; Zhang, W.J. Landslide susceptibility mapping using hybrid random forest with GeoDetector and RFE for factor optimization. *Geosci. Front.* **2021**, *12*, 101211. [CrossRef]
47. Burrough, P.A.; McDonnell, R.A.; Lloyd, C.D. *Principles of Geographical Information Systems*; Oxford University Press: Oxford, UK, 2015.
48. Moore, I.D.; Grayson, R.; Ladson, A.J. Digital terrain modelling: A review of hydrological, geomorphological, and biological applications. *Hydrol. Process.* **1991**, *5*, 3–30. [CrossRef]
49. Chen, X.; Chang, Q.; Guo, B.; Zhang, X.J. Analytical Study of the Relief Amplitude in China Based on SRTM DEM Data. *J. Basic Sci. Eng.* **2013**, *21*, 670–678.
50. Zhang, S.; Li, Z.; Hou, X.; Yi, Y.J.C. Impacts on watershed-scale runoff and sediment yield resulting from synergetic changes in climate and vegetation. *Catena* **2019**, *179*, 129–138. [CrossRef]
51. Wang, X.; Huang, Z.; Hong, M.M.; Zhao, Y.F.; Ou, Y.S.; Zhang, J.J. A comparison of the effects of natural vegetation regrowth with a plantation scheme on soil structure in a geological hazard-prone region. *Eur. J. Soil Sci.* **2019**, *70*, 674–685. [CrossRef]
52. Chen, J.; Ban, Y.; Li, S. China: Open access to Earth land-cover map. *Nature* **2014**, *514*, 434.

53. Piepmeier, J.R.; Focardi, P.; Horgan, K.A.; Knuble, J.; Ehsan, N.; Lucey, J.; Brambora, C.; Brown, P.R.; Hoffman, P.J.; French, R.T.; et al. SMAP L-band microwave radiometer: Instrument design and first year on orbit. *IEEE Trans. Geosci. Remote Sens.* **2017**, *55*, 1954–1966. [CrossRef]
54. Reichle, R.; De Lannoy, G.; Koster, R.; Crow, W.; Kimball, J.; Liu, Q. *SMAP L4 Global 3-Hourly 9 km EASE-Grid Surface and Root Zone Soil Moisture Geophysical Data, Version 5 [Data Set]*; NASA: Boulder, CO, USA, 2020.
55. Breiman, L.J. Random forests. *Mach. Learn.* **2001**, *45*, 5–32. [CrossRef]
56. Stumpf, A.; Kerle, N.J. Object-oriented mapping of landslides using Random Forests. *Remote Sens. Environ.* **2011**, *115*, 2564–2577. [CrossRef]
57. Guzzetti, F.; Carrara, A.; Cardinali, M.; Reichenbach, P.J. Landslide hazard evaluation: A review of current techniques and their application in a multi-scale study, Central Italy. *Geomorphology* **1999**, *31*, 181–216. [CrossRef]
58. Cascini, L.; Fornaro, G.; Peduto, D.J.; Sensing, R. Analysis at medium scale of low-resolution DInSAR data in slow-moving landslide-affected areas. *ISPRS J. Photogramm. Remote Sens.* **2009**, *64*, 598–611. [CrossRef]
59. Bianchini, S.; Herrera, G.; Mateos, R.M.; Notti, D.; Garcia, I.; Mora, O.; Moretti, S.J. Landslide activity maps generation by means of persistent scatterer interferometry. *Remote Sens.* **2013**, *5*, 6198–6222. [CrossRef]
60. Notti, D.; Herrera, G.; Bianchini, S.; Meisina, C.; García-Davalillo, J.C.; Zucca, F.J. A methodology for improving landslide PSI data analysis. *Int. J. Remote Sens.* **2014**, *35*, 2186–2214. [CrossRef]
61. Yunjun, Z.; Fattahi, H.; Amelung, F. Small baseline InSAR time series analysis: Unwrapping error correction and noise reduction. *Comput. Geosci.* **2019**, *133*, 104331. [CrossRef]
62. Notti, D.; Davalillo, J.; Herrera, G.; Mora, O.J.N.H.; Sciences, E.S. Assessment of the performance of X-band satellite radar data for landslide mapping and monitoring: Upper Tena Valley case study. *Nat. Hazards Earth Syst. Sci.* **2010**, *10*, 1865–1875. [CrossRef]
63. Saha, A.; Saha, S.J. Development; Sustainability. Application of statistical probabilistic methods in landslide susceptibility assessment in Kurseong and its surrounding area of Darjeeling Himalayan, India: RS-GIS approach. *Environ. Dev. Sustain.* **2021**, *23*, 4453–4483. [CrossRef]
64. Yu, X. Study on the Landslide Susceptibility Evaluation Method Based on Multi-Source Data and Multi-Scale Analysis. Ph.D. Thesis, China University of Geosciences, Wuhan, China, 2016.
65. Egan, J.P.; Egan, J.P. *Signal Detection Theory and ROC-Analysis*; Academic Press: Cambridge, MA, USA, 1975.
66. Fawcett, T.J. An introduction to ROC analysis. *Pattern Recogn. Lett.* **2006**, *27*, 861–874. [CrossRef]
67. Bradley, A.P. The use of the area under the ROC curve in the evaluation of machine learning algorithms. *Pattern Recognit.* **1997**, *30*, 1145–1159. [CrossRef]
68. Zhao, B.; Dai, Q.; Han, D.; Dai, H.; Mao, J.; Zhuo, L.J. Probabilistic thresholds for landslides warning by integrating soil moisture conditions with rainfall thresholds. *J. Hydrol.* **2019**, *574*, 276–287. [CrossRef]
69. Shen, C.; Feng, Z.; Xie, C.; Fang, H.; Zhao, B.; Ou, W.; Zhu, Y.; Wang, K.; Li, H.; Bai, H.J. Refinement of Landslide Susceptibility Map Using Persistent Scatterer Interferometry in Areas of Intense Mining Activities in the Karst Region of Southwest China. *Remote Sens.* **2019**, *11*, 2821. [CrossRef]